Please cite this article as: Maryami R, Arcondoulis E, Guo, J, Liu, Y (2024). Experimental investigation of active local blowing on the aerodynamic noise reduction of a circular cylinder, *Journal of Sound and Vibration*, 578, 118360. https://doi.org/10.1016/j.jsv.2024.118360

Experimental investigation of active local blowing on the aerodynamic noise reduction of a circular cylinder

Reza Maryami[a], Elias J. G. Arcondoulis[a,b], Jing Guo[a], Yu Liu[a,c,*]

[a] *Department of Mechanics and Aerospace Engineering, Southern University of Science and Technology, Shenzhen, Guangdong 518055, China*
[b] *School of Civil Aerospace and Design Engineering, University of Bristol, BS8 1TR Bristol, Uk*
[c] *Guangdong Provincial Key Laboratory of Turbulence Research and Applications, Southern University of Science and Technology, Shenzhen, Guangdong 518055, China*

Abstract

The strategic implementation of local blowing (LB) around a circular cylinder within a uniform flow has demonstrated its capacity to effectively suppress aerodynamic noise under specific blowing conditions. This study aimed to comprehend the underlying mechanism driving noise reduction through the synchronisation of far-field noise with surface pressure fluctuations, which were measured at various peripheral angles. The parameters under examination for LB were the angle of blowing in relation to the freestream flow (θ_b) and the equivalent momentum coefficient (C_μ). A dedicated series of chambers were employed to facilitate LB at $\theta_b = \pm 41^\circ$, $\pm 90^\circ$, $\pm 131^\circ$, and 180° across the ranges of $C_\mu = 0.007$–0.036 ($Re = 0.7 \times 10^5$) and $C_\mu = 0.003$–0.016 ($Re = 1.04 \times 10^5$). Notably, LB at $\theta_b = \pm 41^\circ$ and 180° exhibited a remarkable reduction in tonal noise within the C_μ range of 0.007 to 0.036. Despite this achievement, the most optimal overall sound pressure level was achieved at $\theta_b = 180^\circ$. It was determined that the dissimilarity in noise reduction among these LB cases was attributed to additional high-frequency noise generated by the blowing technique. The connection between the near- and far-field signals was established through recorded coherence values. The investigation highlighted that surface pressure fluctuations initiated by vortex shedding in the pre- and post-separation regions, particularly at the fundamental vortex shedding frequency, had the most significant impact on far-field noise. The attenuation of such surface pressure fluctuations played a pivotal role in tonal noise reduction by LB, as evidenced by notable reductions in lift fluctuations and the absence of amplitude modulation in both the time and frequency domains.

Keywords: aerodynamic noise, local blowing, circular cylinder, remote-sensing method, surface pressure fluctuations

---

[*] Corresponding author
Email address: `liuy@sustech.edu.cn` (Yu Liu)

1. Introduction

Vortex shedding from a circular cylinder can induce detrimental effects such as structural vibrations, flow-induced noise, and unsteady lift and mean drag forces. These phenomena are encountered in various engineering contexts, including applications like high-speed train pantographs, wind turbine pylons, and landing gears. Consequently, extensive research efforts have been dedicated to understanding the flow dynamics around circular cylinders experiencing vortex shedding over the past decades. In both laminar and turbulent flow conditions, certain previous studies [1–5] have identified a pronounced Aeolian tone linked to the vortex shedding phenomenon. As circular cylinder aerodynamics remains a topic of keen interest, researchers have explored novel flow control strategies aimed at effectively mitigating vortex shedding. A review by Zdravkovich [6] categorised flow control methods into active and passive techniques. Active methods have shown the potential to yield superior performance compared to passive methods, although they necessitate energy input to maintain effective operation [7]. These active techniques allow for real-time manipulation of dynamic and intricate processes during system operation. Some notable examples include inflow oscillations [8], electromagnetic forcing [9], synthetic jets [10], feedback control [11], and thermal effects [12].

Active control strategies encompassing local suction and blowing (LS and LB, respectively) as well as continuous suction and blowing (CS and CB, respectively) have been extensively studied for their potential in actively modulating boundary layer separation and vortex shedding [13–18]. Chen et al. [19] demonstrated through empirical investigations that the precise placement of LS with respect to the incident flow is pivotal in curtailing unsteady load amplitudes. Notably, positioning LS near separation points ($\theta \approx 90^\circ$ and 270°) yielded the most substantial reduction in aerodynamic forces. In a simulation-based analysis, Hu and Liu [20] unveiled that positioning LS within the range of $\theta = \pm 110^\circ$–122.5° led to a remarkable noise reduction of approximately 37.3 dB. Their study also highlighted that LB, when introduced near the cylinder base ($\theta = 180^\circ$), manifested noteworthy noise reduction effects. Furthermore, Deng et al. [21] delved into the effectiveness of LB introduced through a small slot at the cylinder base. Their experimental findings underscored the interaction between symmetric jet vortices and separated shear layers, shedding light on LB's potential for active flow control. In a recent study, Maryami et al. [22, 23] conducted comprehensive flow field measurements, coupled with near-field pressure and far-field noise analysis. Their investigation explored the influence of LB at $\theta = \pm 41^\circ$, $\pm 90^\circ$, and $\pm 131^\circ$, highlighting the remarkable potential of boundary layer LB applications in suppressing near-field pressure and far-field noise by altering the downstream behaviour of vortex shedding. Building on these investigations, Maryami et al. [24, 25] introduced a hybrid approach for mitigating vortex-induced noise. They implemented LB at angles of $\theta = \pm 131^\circ$ and 180° through a structured porous-coated cylinder (SPCC) designed for passive flow and noise control. This innovative hybrid technique yielded significant reductions in both tonal and broadband noise generated by an unmodified cylinder.

Beyond LS and LB, the impacts of CS and CB on wake dynamics, mean drag and lift fluctuations, and flow-induced noise have been briefly explored by other researchers [26–31]. Mathelin et al. [26], in a numerical investigation, noted that CB application tends to augment the boundary layer thickness, induce its separation, decrease the vortex shedding frequency, and reduce viscous drag. Experimental validation of these findings was presented by Fransson et al. [27], who introduced CS and CB via a sintered plastic-coated cylinder surface. Their work further demonstrated that CS leads to separation delay, resulting in a narrower wake width and elevated vortex shedding frequency. The utilisation of CB for mitigating interaction noise was studied

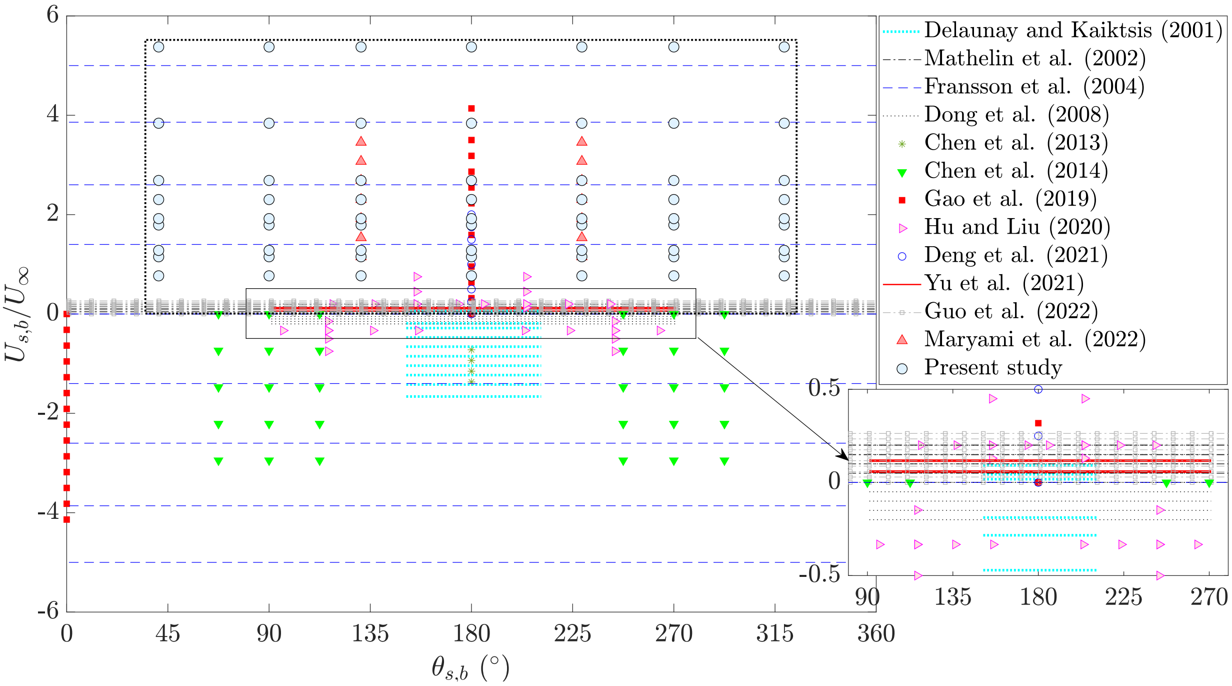

Figure 1: Collection of numerical and experimental data from the literature related to suction and blowing flow control methods applied to a circular cylinder. The $U_{s,b}$ is the suction/blowing velocity and $\theta_{s,b}$ is the peripheral location of the suction/blowing holes. Lines with and without symbols represent CS/CB and symbols depict LS/LB.

by Angland et al. [28], who showcased a noise reduction of 9.2 dB at a Strouhal number of 0.2. More recently, Yu et al. [30] implemented CS on the leeward side of the cylinder using an SPCC. They unveiled the emergence of a regular near-wake characterised by multi-scale coherent structures. Similarly, Guo et al. [31] employed CB through a comparable SPCC design, leading to the damping of wake region fluctuations and a decrease in turbulent kinetic energy.

Exploring strategies to enhance the efficacy of suction and blowing, Dong et al. [32] and Wang et al. [33] proposed a combination of windward CS and leeward CB. Through numerical simulations, they showcased the effectiveness of this approach in eliminating the vortex street and attenuating vortex-induced vibrations. Gao et al. [34] adopted a similar technique, incorporating both LS and LB at the windward and leeward stagnation points, respectively. Their experimental findings demonstrated reductions in drag and fluctuations of dynamic loads exerted on the cylinder. Employing particle image velocimetry, the emergence of blowing vortices was also captured, contributing to the generation of steady and symmetric disturbances.

As outlined earlier, both LS and LB hold substantial promise in mitigating vortex shedding for aerodynamic and aeroacoustic objectives. However, altering critical parameters such as the peripheral hole locations ($\theta_{s,b}$), the spanwise spacing between holes ($L_{0_{s,b}}$), hole size ($d_{0_{s,b}}$), and the active flow rate through holes ($Q_{s,b}$) significantly impacts the performance of these techniques. While a limited number of parametric studies [19, 20, 35] have explored optimal parameter values, there is currently a dearth of experimental investigations providing insights into near-field pressure and far-field noise. Figure 1 presents data from prior research, highlighting the prevalent use of LS and LB at the cylinder base with velocity ratios ($U_{s,b}/U_\infty$) spanning approximately from 0

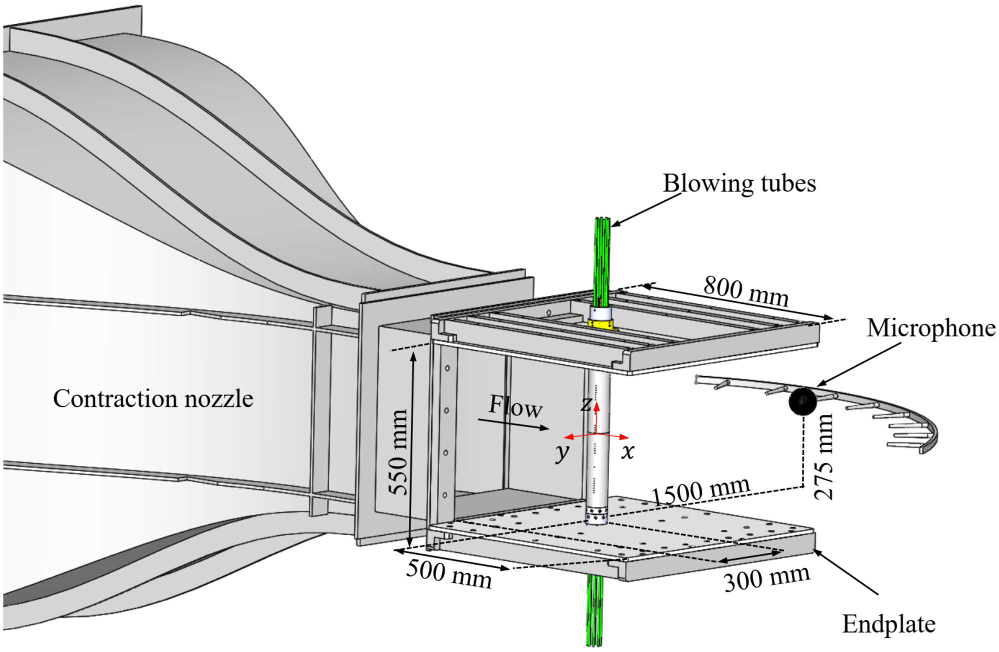

Figure 2: Schematic diagram depicting the experimental setup: the contraction nozzle, the endplates, the placement of the cylinder in the aeroacoustic wind tunnel, and the location of the far-field microphone.

to ±4. Addressing this gap, our present experimental study aims to delve into the influence of hole peripheral locations and the active flow rate of LB (θ_b and Q_b, respectively) on near-field pressure and far-field noise, recognised as key parameters in relevant literature [15, 14, 19, 20, 35]. Our approach involves utilising a circular cylinder equipped with remote-sensing pressure taps to measure surface pressure fluctuations synchronised with far-field noise, thereby offering novel insights in the context of LB. This paper is organised as follows. Section 2 describes the experimental setup including the experimental facility, the cylinder design, the active flow control system, and the measurement technique. The results and discussions are detailed in Sec. 3. Finally, the major findings concerning the application of LB for aeroacoustic applications are summarised in Sec. 4.

2. Experimental setup

2.1. Wind tunnel and experimental facility

The experimental investigations were conducted within a low-speed, closed-loop, open-jet wind tunnel located at Southern University of Science and Technology (SUSTech) [36], as depicted in Fig. 2. The wind tunnel's test section, corresponding to the nozzle exit, boasts a rectangular cross-section measuring 600 mm × 550 mm. This wind tunnel enables flow speeds of up to 70 m/s within the test section, accompanied by an incoming flow turbulence intensity of 0.15%. The aeroacoustic facility encompasses an anechoic chamber with internal dimensions measuring $3.8\ \mathrm{m} \times 5.7\ \mathrm{m} \times 3\ \mathrm{m}$. To maintain a two-dimensional flow over the model, the rectangular endplates, each with a length of 800 mm, are aligned with the nozzle exit. The model itself was positioned vertically between these plates, located at a distance of 300 mm downstream from the nozzle exit. As a result, the model was effectively positioned within the potential core of the nozzle jet flow.

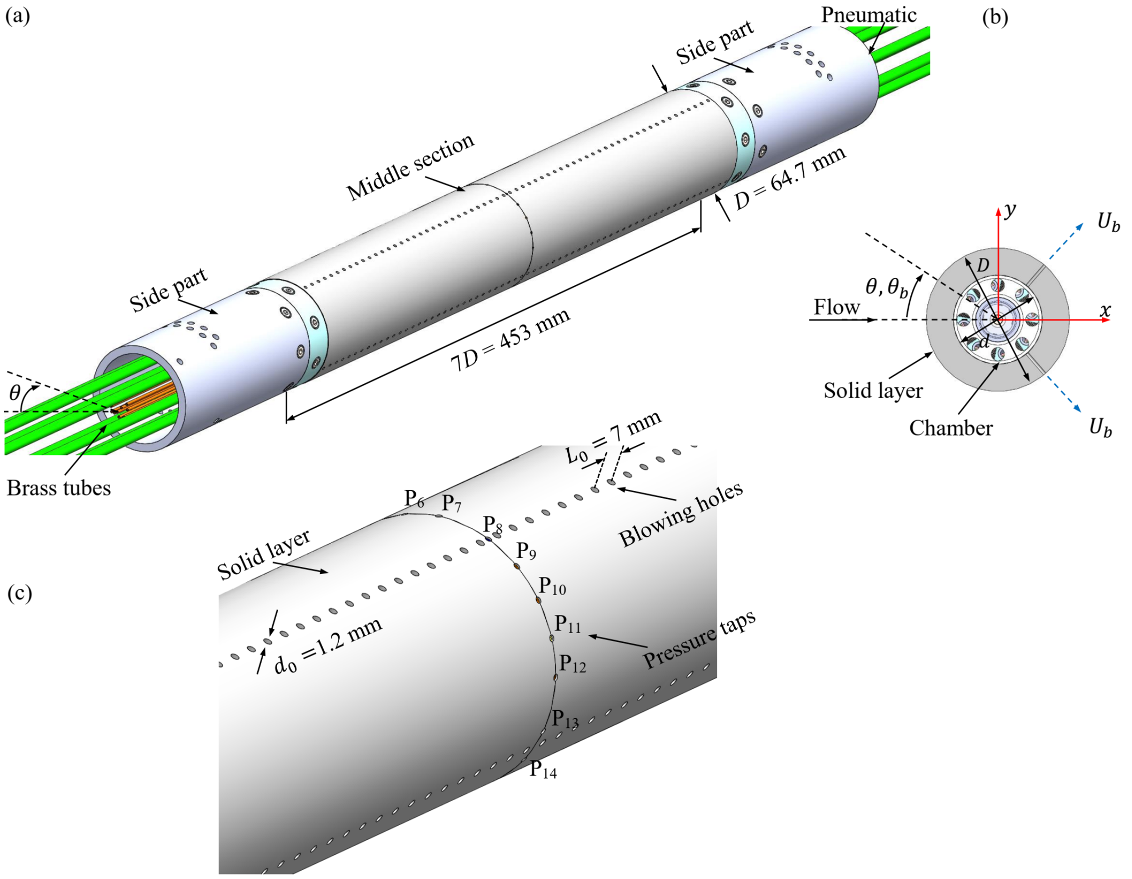

Figure 3: (a) Schematic of the cylinder design, (b) the xy-plane of the cylinder, and (c) the sensing area on the cylinder equipped with remote-sensing pressure taps, P_1–P_{20}, distributed around the circumference of the cylinder at midspan. Note that only pressure taps P_6 to P_{14} are visible here. The peripheral locations of all 20 pressure taps are listed in Table 2.

2.2. Cylinder design

A cylindrical model, characterised by an outer diameter of $D = 64.7$ mm and a span of $L = 550$ mm, was originally designed by Maryami et al. [22]. The model featured three distinct parts spanning its length: a middle section equipped with pressure taps and chamber instrumentation, flanked by two side extension parts, as illustrated in Figure 3(a). Several crucial factors were taken into account to determine the optimal outer diameter for the cylinder. These factors encompassed the blockage ratio, aspect ratio, and potential effects of low-frequency background noise. Through careful consideration, an outer diameter of 64.7 mm was chosen, resulting in a blockage ratio of less than 12%. The aspect ratio of the cylinder stood at approximately 8.5, indicating that any potential influence from the endplates could be disregarded [6]. For the experimental conditions, the incoming flow velocity was set at $U_\infty = 20$ and 30 m/s, corresponding to diameter-based Reynolds numbers of $Re = 0.7 \times 10^5$ and 1.04×10^5, respectively.

The middle section of the cylinder model was layered with a sequence of solid layers, featuring cylinders with inner and outer diameters of $d = 40$ mm and $D = 64.7$ mm, respectively. These layers were equipped with holes of diameter $d_0 = 1.2$ mm, permitting the application of distributed LB across the cylinder's surface. Within this study, LB was executed at specific angles, namely

$\theta_b = \pm 41°$, $\pm 90°$, $\pm 131°$, and 180°, utilising an open-loop control strategy. These designated scenarios, denoted as LB41, LB90, LB131, and LB180, correspond respectively to the boundary layer, the shear layers on the cylinder, the separated shear layers, and the wake region near the base of the cylinder. Depending on the LB configuration, the blowing holes were distributed along either one or two lines, situated in the upper and lower halves of the cylinder, maintaining a spanwise spacing of $L_0 = 7$ mm. As prior experimental data in the literature have indicated that the maximum spanwise coherence length of a circular cylinder varies within the range of $3.3D$–$3D$ [37] in this Reynolds number domain, a total of 64 holes were evenly positioned across a span length of $7D$. This approach ensured the establishment of a comprehensive three-dimensional (3-D) flow field along the span of the cylinder.

Four 3-D printed chambers were strategically designed to implement LB at various angles around the cylinder. Each chamber was securely integrated into the corresponding solid layer, as illustrated in Fig. 3(*b*), ensuring proper alignment between the chamber holes and those in the solid layer. This arrangement was aimed at achieving a more even distribution of LB along the span. To assess the uniformity of LB distribution across the span, the static pressure distribution was measured using steel tubes with inner and outer diameters of 0.5 mm and 1 mm, respectively, similar to Maryami et al. [22]. These tubes were inserted into the chamber holes and connected to 16-channel Model 9116 Intelligent Pressure Scanners through flexible tubes featuring an inner diameter of 0.5 mm and an outer diameter of 2 mm. The outcomes indicated that the pressure across the chamber span remained consistent within ±0.1%, as previously demonstrated in Ref. [22]. Additionally, the chamber was divided at the half-span of the cylinder to accommodate remote-sensing pressure taps. Hence, LB was applied to both sides of the chamber, with each side being supplied by eight inlets for tube connections. The LB flow rate was quantified using a mass flow meter and maintained at a constant level via a regulator and pressure gauge. The utilisation of the equivalent momentum coefficient, C_μ, facilitated the investigation. This coefficient, previously employed in references such as [16, 19, 21, 22, 34], is defined as the ratio of the LB momentum flux at each hole to the incoming flow momentum flux and is defined as follows:

Table 1: LB flow rate, Q_b, velocity ratio, U_b/U_∞, and corresponding C_μ values calculated using Eq. (1).

$Q_b(\mathrm{m}^3/\mathrm{h})$ LB180	$Q_b(\mathrm{m}^3/\mathrm{h})$ LB41, LB90, LB131	U_b/U_∞ LB180	U_b/U_∞ LB41, LB90, LB131	$U_\infty(\mathrm{m/s})$	C_μ
8.5	12	1.09	0.77	30	0.0030
8.5	12	1.63	1.15	20	0.0070
14	20	1.80	1.28	30	0.0080
20	28	2.53	1.80	30	0.0160
14	20	2.77	1.90	20	0.0185
20	28	3.80	2.70	20	0.0360

$$C_\mu = \left(\frac{U_b}{U_\infty}\right)^2 \left(\frac{A_b}{DL_0}\right) \tag{1}$$

where U_b denotes the average LB velocity at each hole, L_0 signifies the spacing between neighbouring blowing holes along the span (see 3(*b*)), and A_b represents the combined area of the blowing holes at each section. Note that LB41, LB90, and LB131 utilised two holes at each section, one on the upper and one on the lower sides of the cylinder. In contrast, LB180 featured

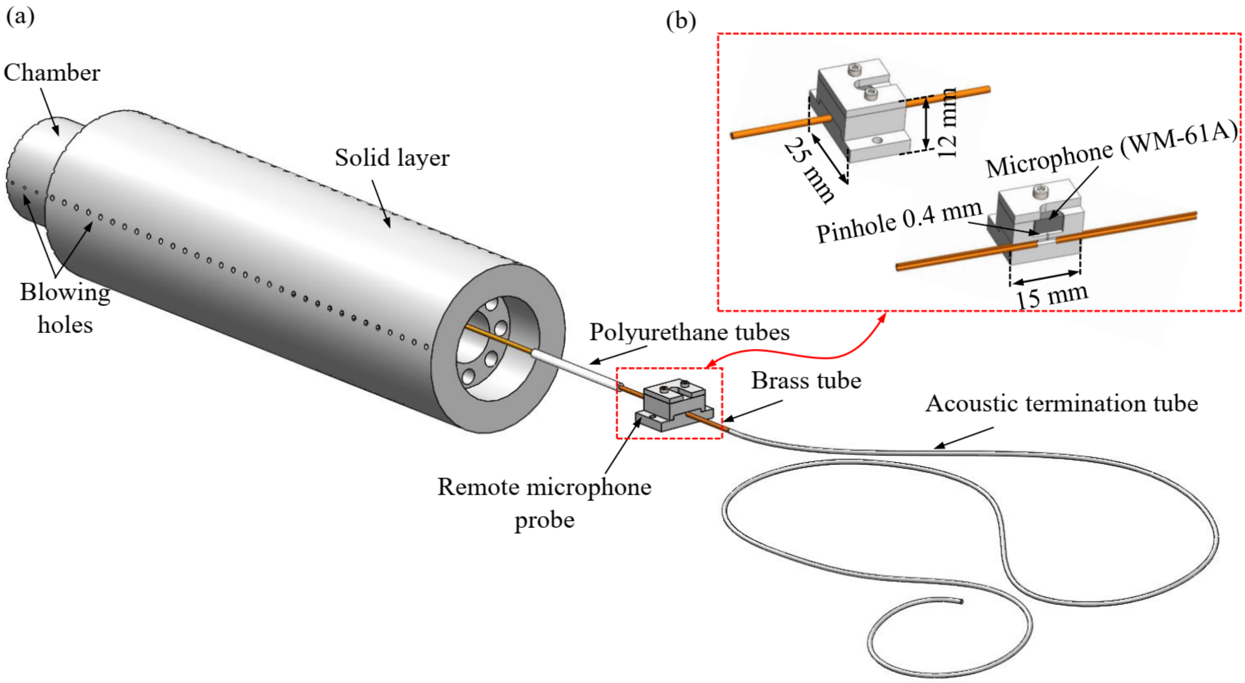

Figure 4: (*a*) Full view of the remote-sensing setup and (*b*) assembly view of the remote-sensing holder.

only one hole at each section, positioned at the base of the cylinder. Referring to the compiled data in Fig. 1, it is evident that U_b/U_∞ typically remains under 5. Consequently, this upper limit was utilised to establish the range of C_μ in the current study. The values of Q_b, U_b/U_∞, and their corresponding C_μ are outlined in Table 1. Notably, the experimental trials were conducted employing three LB flow rates of 12, 20, and 28 m^3/h, with the exception of LB180, where the rates were adjusted to 8.5, 14, and 20 m^3/h, respectively, to maintain consistent C_μ values.

2.3. Near-field pressure and acoustic measurements

A remote-sensing approach was employed for near-field pressure measurements using pressure taps integrated into the middle section of the cylinder, as illustrated in Fig. 3(*c*). Within this segment, the cylinder was outfitted with 20 pressure taps, distributed with non-uniform angular intervals, as summarised in Table 2. These pressure taps were connected to brass tubes with inner and outer diameters of 0.8 mm and 1.6 mm, respectively. These brass tubes were further linked to the remote-sensing probes using brass and flexible polyurethane tubing with inner and outer diameters of 0.8 mm and 4 mm, respectively, mirroring the approach of Maryami et al. [22, 38, 39]. The remote sensing probes, as depicted in Fig. 4, featured a Panasonic WM-61A microphone, with a circular sensing diameter of 2 mm, affixed to a pinhole with a 0.4 mm diameter. To alleviate spurious tones related to standing waves in the flexible tubing, an extension tube of 2 m was appended to the microphone holder's brass tube. The reliability of Panasonic WM-61A microphones in providing accurate pressure data within the frequency range of interest ($20\,\mathrm{Hz} \leq f \leq 10\,\mathrm{kHz}$) has been demonstrated in prior studies [3–5, 22, 38, 40–42].

For *in-situ* calibration, a custom-designed calibrator was employed, following a similar approach as used by Maryami et al. [3]. This bespoke calibrator was conceptualised and constructed as an integral component of the research. It comprised a high-quality loudspeaker, linked to a cone-shaped extension featuring a 110 mm long tube with a 10 mm diameter, a reference microphone holder, and an acoustic termination tube. A 1/2 inch Brüel & Kjær (B&K) free-field microphone Type 4966 served as the reference microphone, calibrated using a B&K calibrator Type 4231. Both remote-sensing probe and the reference microphone were exposed simultaneously to a white noise signal generated by the loudspeaker. A transfer function, denoted as T_{RM}, characterising the relationship between the remote-sensing probe and the reference microphone was calculated via

$$T_{RM}(f) = \frac{\phi_{MM}(f)}{\phi_{RM}(f)} \tag{2}$$

where ϕ_{MM} is the auto-spectrum of the remote-sensing signals and ϕ_{RM} is the cross-spectrum between the reference and remote-sensing signals. Note that both the reference and remote-sensing pressure measurements were conducted simultaneously. The coherence values between these pressure signals were consistently high, approximating one for frequencies equal to or less than approximately 6 kHz. It is important to note that this frequency corresponds to $St \approx 13$ at an incoming flow velocity of $U_\infty = 30$ m/s. This value is sufficiently elevated for the frequency range of interest in the present study, and aligns with the upper-frequency range observed in other studies [22, 43–45].

Table 2: Peripheral positions of the pressure taps at $z/D = 0$. θ is defined in Fig. 3(b).

Pressure taps	$\theta(^\circ)$	Pressure taps	$\theta(^\circ)$
P1	0	P11	180
P2	17	P12	−164
P3	41	P13	−131
P4	57	P14	−123
P5	74	P15	−107
P6	90	P16	−90
P7	107	P17	−74
P8	131	P18	−41
P9	147	P19	−33
P10	164	P20	−17

Far-field noise measurements were conducted employing a B&K free-field Type 4966 microphone, positioned at an angle of 90° to the flow and situated 1.5 meters from the cylinder axis, as illustrated in Fig. 2. The acquisition of near-field pressure and far-field noise was simultaneous, utilising a National Instruments (NI) PXI-10420 chassis housing two synchronised NI PXI-4496 data acquisition cards. A sampling frequency of 51.2 kHz was employed for data collection, performed over a span of 10 seconds. The 10-second measurement duration ensures a stable airflow without requiring compressor restarts. The pressure-time data were transformed into the frequency domain using Fast Fourier Transformation (FFT) with Hamming windowing, incorporating 50% overlap through Welch's method. This approach yielded a frequency resolution of 2 Hz. The transformed data were subsequently converted into Power Spectral Density (PSD), denoted as $\phi_{pp,s}$ and ϕ_{pp} (dB/Hz), corresponding to the near-field and far-field pressures, respectively. For every remote sensing probe, the $\phi_{pp,s}$ were divided by T_{RM}^2. This adjustment aimed to account for phase delays and amplitude attenuation introduced by the remote sensing setup.

To quantify the error in $\phi_{pp,s}$ and ϕ_{pp} spectra, it is crucial to consider various factors such as frequency sampling, recording time, sub-blocks, window size, and overlap. Following the estimation methods for convergence error in Fourier transform [46], this study analysed the random error. Utilising 26 sub-blocks results in an error of about 0.76 dB for both $\phi_{pp,s}$ and ϕ_{pp}, as determined by $10\log_{10}(1+1/\sqrt{N_b})$, where N_b is the number of sub-blocks. In addition, the confidence intervals at a 95% confidence level for $\phi_{pp,s}$ and ϕ_{pp} at the vortex shedding frequency were estimated as [-0.85 dB, 0.71 dB] and [-0.15 dB, 0.16 dB], respectively.

3. Results

3.1. Far-field spectra

The acoustic PSD, Φ_{pp} (dB/Hz), results of each LB are presented in Fig. 5 against Strouhal number, $St = fD/U_\infty$, for $Re = 0.7 \times 10^5$ and 1.04×10^5. The PSD data are referenced to $p_0 = 20\ \mu$Pa as follows

$$\Phi_{pp} = 10\log_{10}\left(\frac{\phi_{pp}}{p_0^2}\right) \tag{3}$$

At a Reynolds number of $Re = 0.7 \times 10^5$, the baseline exhibits the fundamental vortex shedding tone (f_1) with a St of approximately 0.19. This f_1-tone is also referred to as the first harmonic, while other tones with frequencies that are positive integer multiples of the fundamental frequency are known as higher harmonics ($f_2 = 2f_1$, $f_3 = 3f_1$, ...). Among all LB cases at $C_\mu = 0.007$, as shown in Fig. 5(a), there is a reduction in tonal noise, except for LB90. Both LB41 and LB180 demonstrate a comparable reduction of approximately 19 dB, making them the best-performing cases in this regard. LB41 displays a dual vortex shedding tone phenomenon, particularly at $C_\mu = 0.007$. Although the exact cause of this dual tone remains uncertain, it is likely attributed to the interaction between the blowing-induced perturbations in the boundary layer and the shedding of vortices from the cylinder surface. One peak in the PSD corresponds to the f_1-tone frequency ($St \approx 0.25$), while the other peak at $St \approx 0.2$ is associated with the frequency of perturbations introduced by the blowing in the boundary layer, influencing the shear layer disturbances for another vortex shedding at a frequency close to the fundamental one. This dual peak phenomenon aligns with the observations made by Showkat Ali et al. [47], who suggested its relation to the presence of two types of vortical structures in the wake region. The peak at $St \approx 0.2$ may also be attributed to nonlinear interactions between vortex shedding and boundary layer perturbations induced by LB41, along with resonance effects due to modified acoustic modes caused by LB41.

From Figs. 5(a)–5(c), it becomes evident that each LB case reduces tonal noise as C_μ increases. At $C_\mu = 0.036$, the f_1-tone weakens significantly, registering $\Phi_{pp} \approx 45$ dB (a 23 dB reduction from the baseline) at the f_1-tone frequency for LB180, while LB41 exhibits this tone with a magnitude around 48 dB. In terms of broadband noise, there is no observable reduction for LB41 and LB90, and their spectral content remains roughly similar to that of the baseline within the range of $St \approx 0.2$ to 1. For LB131 and LB180, the characteristics of broadband noise are similar, and a reduction in spectral content is noticeable within $St \approx 0.15$–2 across the range of $C_\mu = 0.007$–0.036. However, a distinct contribution of strong broadband noise relative to the baseline becomes noticeable within $St \approx 2$–13, which can be directly attributed to the blowing self-noise and has been substantiated by the findings of others [24, 28, 48]. Identifying the precise components of the blowing system responsible for this noise proves to be a challenge. Nonetheless, it is evident that both the

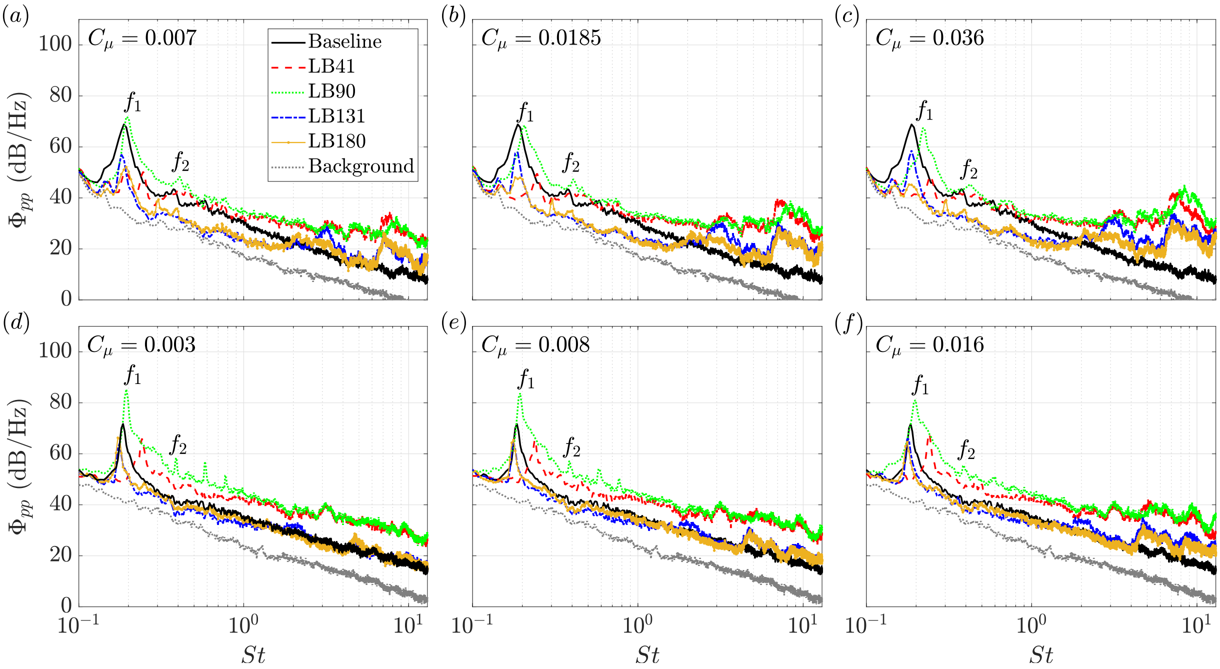

Figure 5: Acoustic PSD, Φ_{pp} (dB/Hz), plotted against St for various C_μ values and LB cases. (*a*–*c*) $Re = 0.7 \times 10^5$ and (*d*–*f*) $Re = 1.04 \times 10^5$.

compressor and chamber play roles in the generation of self-noise. A previous study [28] underscores that the principal noise emerges from the chamber and the blowing holes when the air is delivered to the free field. Moreover, Angland et al. [28] demonstrated that the adoption of a sintered plate with a very small pore diameter can mitigate the additional noise associated with CB. It is important to highlight that the ratio of vortex shedding noise to blowing self-noise is considerably high, as previously reported by Maryami et al. [22] and Guo et al. [48] in their study using the same air supply system at SUSTech and similar air flow rates. This significant ratio is crucial in enabling the investigation of the effects of LB on the suppression of vortex shedding noise from a circular cylinder.

Upon elevating the Reynolds number to $Re = 1.04 \times 10^5$, which corresponds to the lower C_μ values compared to those at $Re = 0.7 \times 10^5$, it remains evident that each LB case, except for LB90, still demonstrates some level of reduction in the f_1-tone across the entire span of C_μ, as depicted in Figs. 5(*d*)–5(*f*). However, the effectiveness of these LB cases in diminishing the magnitude of the f_1-tone is somewhat diminished compared to the results observed at $Re = 0.7 \times 10^5$. For LB90, the magnitude of this tone continues to exceed that of the baseline as C_μ is increased from 0.003 to 0.016. This underscores the fact that, at each value of C_μ for $Re = 1.04 \times 10^5$, every LB case continues to exhibit a prominent f_1-tone. This outcome underscores the notion that none of the investigated LB techniques is fully capable of eradicating the mechanism responsible for generating vortex shedding noise.

With regard to broadband noise, both LB41 and LB90 exhibit an increase in spectral content beyond $St \approx 0.2$, whereas LB131 and LB180 demonstrate the same spectral content as the baseline. At $Re = 1.04 \times 10^5$, the spectral behaviour of LB does not demonstrate significant variation concerning the relatively small values of C_μ. This suggests that the free flow's impact on the flow field around and behind the cylinder outweighs the influence of LB rate. Figure 5 indicates that the vortex shedding Strouhal number shifts either lower or higher than that of the baseline, contingent on the LB angle. At $Re = 1.04 \times 10^5$, LB41 and LB90 introduce an f_1-tone at $St \approx 0.24$ and 0.19, respectively, yet this shifts to around 0.17 for the other LB cases.

In order to gain a better understanding of the tonal noise reduction of LB with respect to C_μ, Φ_{pp} of the LB cases are normalised relative to Φ_{pp} of the baseline at their respective f_1-tone frequency, i.e., $\Delta\Phi_{pp}|_{f_1}$ (dB/Hz), and is calculated as

$$\Delta\Phi_{pp}|_{f_1} = 10\,\log_{10}\left(\frac{\phi_{pp}|_{f_1,\mathrm{LB}}}{\phi_{pp}|_{f_1,\mathrm{Baseline}}}\right) \tag{4}$$

Figure. 6(a) illustrates that all LB cases, except for LB90, exhibit tonal noise reduction ($\Delta\Phi_{pp}|_{f_1} < 0$) across the considered range of Reynolds numbers and C_μ values. The reduction in tonal noise is attributed to the size of the vortex formation region, as demonstrated more recently by Maryami et al. [22]. Their detailed findings indicate that delaying the rolling up of the shear layers allows for their mutual interaction to occur further downstream, leading to an enlarged vortex formation size. Consequently, the reduction in turbulent kinetic energy near the cylinder aligns with the suppression of near-field pressure and far-field noise at the f_1-tone frequency. At $Re = 0.7 \times 10^5$, LB41 and LB180 demonstrate superior tonal noise reduction, with the latter showing a 3 dB reduction more than the former at $C_\mu = 0.036$. At $Re = 0.7 \times 10^5$, the behaviour of LB41 and LB131 in reducing the magnitude of the f_1-tone compared to the baseline remains relatively consistent across different C_μ values. On the other hand, LB90 and LB180 exhibit a substantial reduction in magnitude from $C_\mu = 0.007$ to 0.036. The noise suppression efficiency of each LB case against vortex-induced noise appears to decrease with increasing Reynolds number. At $Re = 1.04 \times 10^5$, all LB cases except for LB90 showcase a consistent reduction in the f_1-tone magnitude, ranging approximately between 5 and 8 dB, which remains nearly constant across various C_μ values. For most C_μ values, LB131 demonstrates a slightly higher reduction in the f_1-tone magnitude compared to other LB cases. Conversely, LB90 shows an increase in the magnitude of the f_1-tone relative to the baseline. This increase is approximately 14 dB at $C_\mu = 0.003$, and it decreases to around 9 dB at $C_\mu = 0.016$. One possible mechanism for this phenomenon could be the acceleration of vortex shedding (resulting in a smaller vortex formation size), which contribute to the elevated magnitude of the f_1-tone in the case of LB90 [22].

In the subsequent discussion, we will delve into the impacts of LB on the shift in the vortex shedding Strouhal number. The normalised Strouhal numbers of the LB cases, denoted as $St/St_{\mathrm{Baseline}}$, are depicted in Fig. 6(b). It is worth noting that the baseline Strouhal number remains approximately constant ($St \approx 0.19$) across the range from $Re = 0.7 \times 10^5$ to 1.04×10^5, consistent with existing published data [37]. It is observed that LB41 and LB90 consistently exhibit $St/St_{\mathrm{Baseline}} > 1$ across all Reynolds numbers and values of C_μ. On the contrary, the behaviour is opposite for the remaining LB cases. Irrespective of the specific LB case, there is a general decrease in $St/St_{\mathrm{Baseline}}$ with increasing Reynolds number. Additionally, at a given Reynolds number, the value of $St/St_{\mathrm{Baseline}}$ remains relatively constant across different C_μ values for most of the LB cases. For LB90, a substantial increase in $St/St_{\mathrm{Baseline}}$ with C_μ is only apparent at $Re = 0.7 \times 10^5$. Upon observing Fig. 6(b), it becomes apparent that $St/St_{\mathrm{Baseline}}$ tends to decrease as θ_b is increased from ±41° to 180° across the range of Reynolds numbers and C_μ values, with certain exceptions at $C_\mu = 0.007$. At this specific C_μ, the value of $St/St_{\mathrm{Baseline}}$ for $\theta_b = \pm 131°$ is notably smaller than that corresponding to $\theta_b = 180°$.

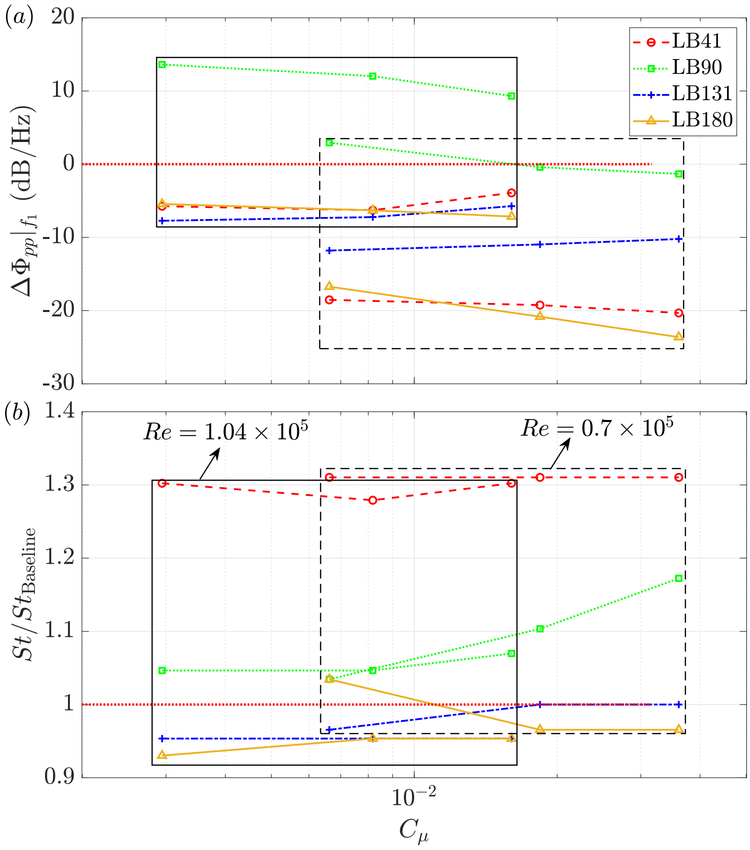

Figure 6: (*a*) Normalised acoustic PSD at the f_1-tone frequency, $\Delta\Phi_{pp}|_{f_1}$ (dB/Hz) and (*b*) normalised Strouhal number, St/St_{Baseline}, as a function of C_μ. The Reynolds numbers $Re = 0.7 \times 10^5$ and 1.04×10^5 are denoted by dashed and solid rectangles, respectively.

The overall sound pressure level (OASPL) for the LB cases in comparison to the baseline, denoted as ΔOASPL (dB), was determined by integrating the far-field PSD across the entire frequency range of interest, which corresponds to approximately $St \approx 0.13$–13. This calculation was performed using the following formula:

$$\Delta\text{OASPL} = 10\,\log_{10}\left(\frac{\int \phi_{pp}|_{\text{LB}}\;\mathrm{d}f}{\int \phi_{pp}|_{\text{Baseline}}\;\mathrm{d}f}\right) \tag{5}$$

The fundamental trends, as already observed in Fig. 6(*a*), highlight that both LB41 and LB180 exhibit favourable characteristics in reducing tonal noise, exhibiting similar behaviour to each other at $Re = 0.7 \times 10^5$. However, a closer examination of the ΔOASPL values in Fig. 7(*a*) reveals that LB180 has a more pronounced effect in controlling noise compared to the other LB cases. This difference in noise control effectiveness, especially in comparison to LB41, can likely be attributed to the influence of self-noise.

To discern the influence of self-noise on OASPL, the far-field PSD was integrated over a frequency range corresponding to $St \approx 2$–13, which is likely dominated by self-noise contributions, as evident in Fig. 5. These outcomes are presented in Fig. 7(*b*), where it becomes apparent that self-noise levels increase for each LB case with varying C_μ while maintaining a constant Reynolds

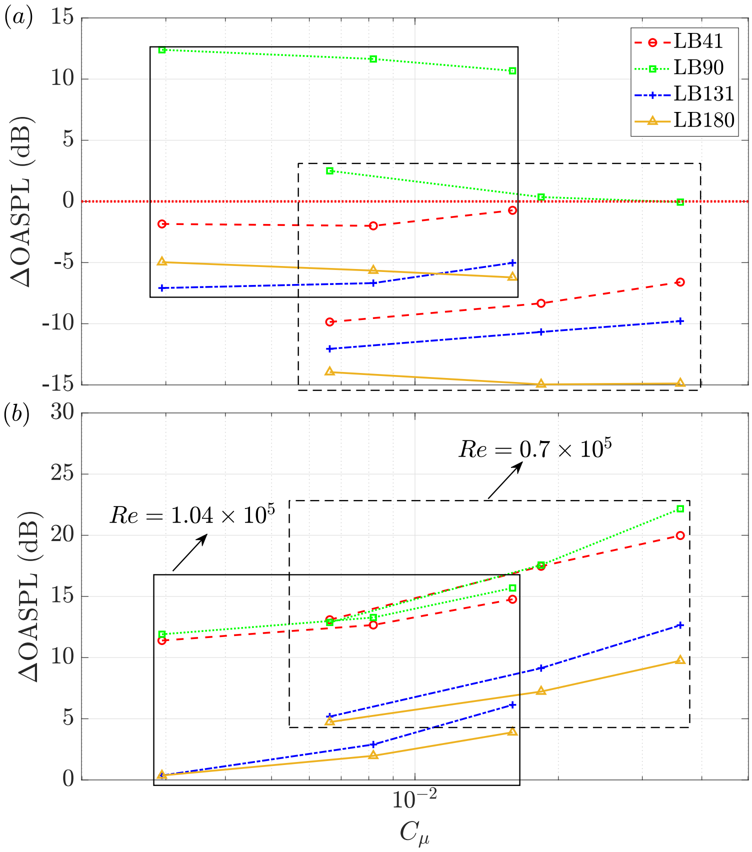

Figure 7: ΔOASPL (dB) for each LB integrated over frequency ranges corresponding to (*a*) $St \approx 0.13$–13 and (*b*) $St \approx 2$–13. The Reynolds numbers $Re = 0.7 \times 10^5$ and 1.04×10^5 are denoted by dashed and solid rectangles, respectively.

number. This trend indicates that this noise contribution is associated with the LB technique. Furthermore, within the range of Reynolds numbers, LB180 consistently exhibits a lower level of self-noise compared to the other LB cases. In contrast, LB41 and LB90, demonstrating a similar pattern, tend to produce higher levels of self-noise. A careful observation of Figs. 7(*a*) and 7(*b*) highlights the results from LB180, reaffirming the significance of minimising self-noise contributions in noise reduction applications. This notion is in line with the findings of Angland et al. [28], emphasising the necessity for a well-designed blowing system to ensure that any additional noise remains within a high-frequency range where it can be subject to atmospheric attenuation. Notably, atmospheric attenuation is more effective in the high-frequency spectrum compared to the lower frequencies where the bulk of aerodynamic noise is generated [28, 49].

3.2. Near-field pressure spectra

The near-field pressure PSD, $\Phi_{pp,s}$ (dB/Hz), was calculated by Eq. (5) and the results at some angles, i.e., $\theta = 0°$, $41°$, $90°$, $131°$, and $180°$, are presented in Fig. 8. It should be noted that C_μ increases from 0.003 to 0.036 yet it is not necessarily due to an increase in Q_b between 12 and 28 m^3/h; the Reynolds number also varies from $Re = 1.04 \times 10^5$ to 0.7×10^5, respectively. The baseline case exhibits a dominant tonal peak at the f_1-tone frequency, consistent with the fundamental vortex shedding tone observed in Fig. 5. This confirms that the surface pressure fluctuations are primarily caused by vortex shedding and serve as the acoustic source [22, 38, 50]. In line with the findings of Maryami et al. [22], the far-field noise is mainly generated by alternating pressure pulses induced on both sides of the cylinder during the intermittent shedding of vortices. These pressure pulses result from shear layer interactions and rapid vertical flow movements in the vortex formation region.

From Figs. 8(a_1) and 8(b_1) at $\theta = 0°$, the baseline shows weak f_1- and f_2-tones. At $C_\mu = 0.003$ as shown in Fig. 8(a_1), LB41 shows an absence of these tonal peaks, while LB180 mirrors a magnitude at the same level as the baseline. For these LB cases, a high broadband contribution compared to the baseline is initiated at $St \gtrapprox 0.5$ and 1, respectively. In contrast, LB90 and LB131 exhibit strong f_1-tones, with magnitudes approximately 11 and 18 dB larger than the baseline, respectively. Additionally, for these LB cases, the broadband spectral content increases compared to the baseline at $St \gtrapprox 0.2$. It is worth noting that LB90 displays the first three harmonics (f_2, f_3, and f_4), with the even harmonics stronger than the odd harmonics, indicating an increase in drag fluctuations. Further discussions on lift and drag fluctuations occurring at odd and even harmonics (i.e., f_1, $3f_1$, ... and $2f_1$, $4f_1$, ...), respectively, will be presented in Sec. 3.3, as reported in previous studies [2, 4, 5, 22, 40, 51, 52]. When C_μ is increased to 0.036 (see Fig. 8(b_1)), LB180 exhibits a behaviour similar to that of LB41, effectively eliminating the tonal peaks. In these cases, the broadband spectral content remains lower than that of the baseline up to $St \approx 2$, after which the opposite trend emerges. Similar to the observations at $C_\mu = 0.003$, for LB90 and LB131 cases, the magnitude of the f_1-tone is still larger compared to that of the baseline, although the difference decreases to 9 and 12 dB, respectively. In relation to broadband spectral content, these cases exhibit an increase relative to the baseline beyond $St \approx 1$.

At $\theta = 41°$ away from the stagnation point (see Figs. 8(a_2) and 8(b_2)), the f_1-tone is observed for all LB cases. Additionally, each LB case, except for LB41, exhibits the f_2-tone, which disappears completely when C_μ is increased to 0.036. At $C_\mu = 0.003$, as shown in Fig. 8(a_2), LB41 reduces the f_1-tone magnitude by approximately 26 dB relative to the baseline, achieving the best performance among the LB cases. In contrast, LB90 exhibits a strong f_1-tone, exceeding the magnitude of the baseline by around 7.5 dB, indicating strong lift fluctuations (see Fig. 11). LB131 and LB180 produce similar f_1-tones, approximately 9 dB smaller than that of the baseline. In Fig. 8(a_2), each LB case, except for LB180, exhibits a high broadband contribution relative tot he baseline for $St \gtrapprox 0.4$. LB180 also displays this contribution, but it initiates from $St \approx 1$, indicating a lower broadband spectral content compared to the other LB cases. By increasing C_μ to 0.036, the effectiveness of all LB cases in suppressing the near-field pressure at the f_1-tone frequency improves (see Fig. 8(b_2)). It is observed that every LB case, even LB90, is able to reduce the f_1-tone magnitude from that of the baseline. Among them, LB41 exhibits the greatest reduction by around 28 dB, while LB90 shows a reduction of only 5.5 dB. At this C_μ value, the broadband spectral content is reduced by every LB case except LB41 when compared to what was observed at $C_\mu = 0.003$. This trend is especially pronounced in the cases of LB131 and LB180, where they exhibit a reduction relative to the baseline up to $St \approx 2$. LB41 and LB90 showcase a broadband contribution compared to the baseline starting around $St \approx 0.4$, much like the behaviour observed at $C_\mu = 0.003$. However, in the cases of LB130 and LB180, this broadband contribution initiates at $St \approx 2$, with LB180 exhibiting the lowest contribution among all the LB cases.

At positions further away from the stagnation point, specifically at $\theta = 90°$ and 131°, the magnitude of the f_1-tone increases for each LB case. However, LB41 continues to outperform

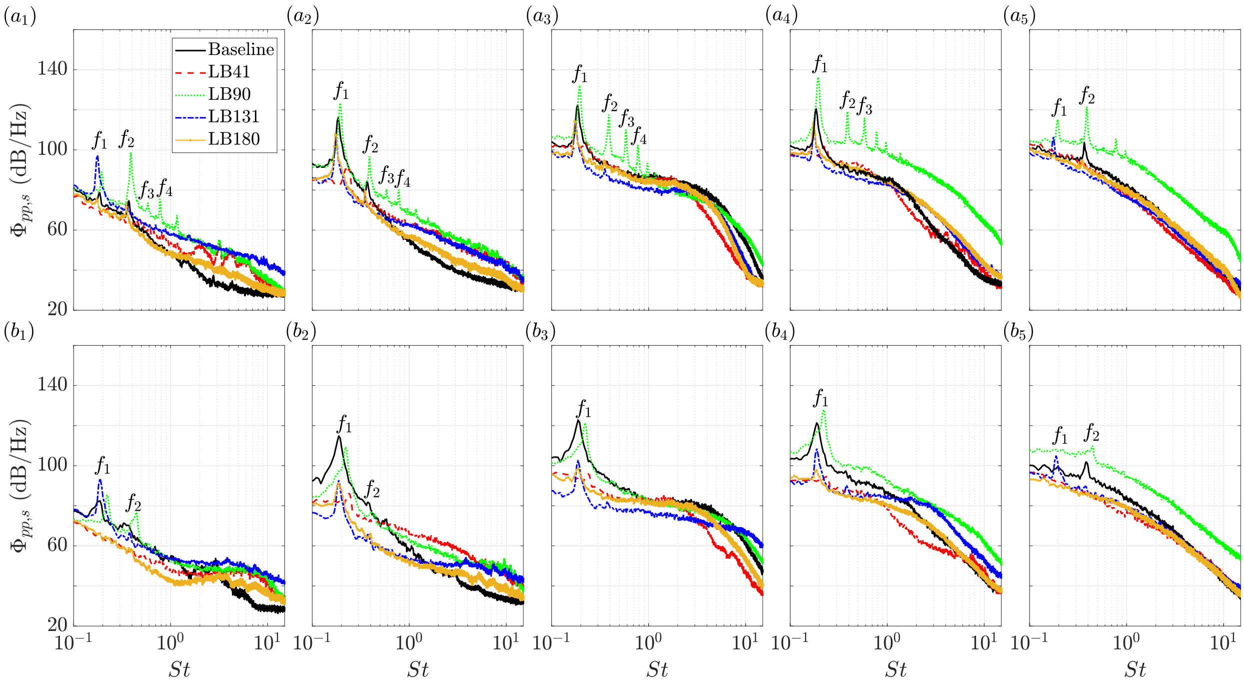

Figure 8: Near-field PSD, $\Phi_{pp,s}$ (dB/Hz), at (a_1, b_1) $\theta = 0°$, (a_2, b_2) 41°, (a_3, b_3) 90°, (a_4, b_4) 131°, and (a_5, b_5) 180°. (a_1–a_5) $C_\mu = 0.003$ ($Re = 1.04 \times 10^5$) and (b_1–b_5) $C_\mu = 0.036$ ($Re = 0.7 \times 10^5$).

other cases in terms of reducing this magnitude from that of the baseline, while the opposite trend is observed for LB90. In contrast to $\theta = 41°$, at $\theta = 90°$, there is no significant high broadband contribution compared to the baseline. For $St \gtrapprox 2$, some LB cases, particularly LB41, reduce the broadband spectral content compared to that of the baseline. At $\theta = 131°$, the LB cases generally exhibit a similar behaviour to that observed at $\theta = 41°$, with some exceptions. As the C_μ value increases, the performance of all LB cases in suppressing the tonal and broadband components of the near-field pressure at $\theta = 90°$ and 131° improves, particularly notable in the case of LB90. For instance, at $\theta = 90°$ as shown in Figs. 8(a_3) and 8(b_3), which corresponds to the cylinder's shoulders, LB90 exhibits the f_1-tone with an amplitude of approximately 120 dB at $C_\mu = 0.036$, as opposed to 132 dB at $C_\mu = 0.003$.

At $\theta = 180°$, as depicted in Figs. 8(a_5) and 8(b_5), LB41 and LB180 predominantly exhibit broadband characteristics across the entire Strouhal number range, with no discernible broadband contribution compared to the baseline. In the case of LB90 and LB131, the tonal behavior is somewhat similar to that observed at $\theta = 0°$. LB90 demonstrates a significant broadband contribution over the whole range of Strouhal number, while LB131 shows the broadband spectral content at a level similar to the baseline, particularly at high Strouhal numbers. With an increase in C_μ, the effectiveness of all flow control methods in mitigating the near-field pressure at $\theta = 180°$ enhances. LB90, in particular, demonstrates improvement across the entire Strouhal number range, whereas for the others, it is noticeable up to $St \approx 3$.

Figure 9 illustrates the peripheral variation of the maximum surface pressure spectra at the f_1- and f_2-tone frequencies, denoted as $\Phi_{pp,s}|_{f_1}$ and $\Phi_{pp,s}|_{f_2}$ (dB/Hz), respectively. Upon casual observation, all cases display an approximately symmetric directivity pattern for the f_1- and

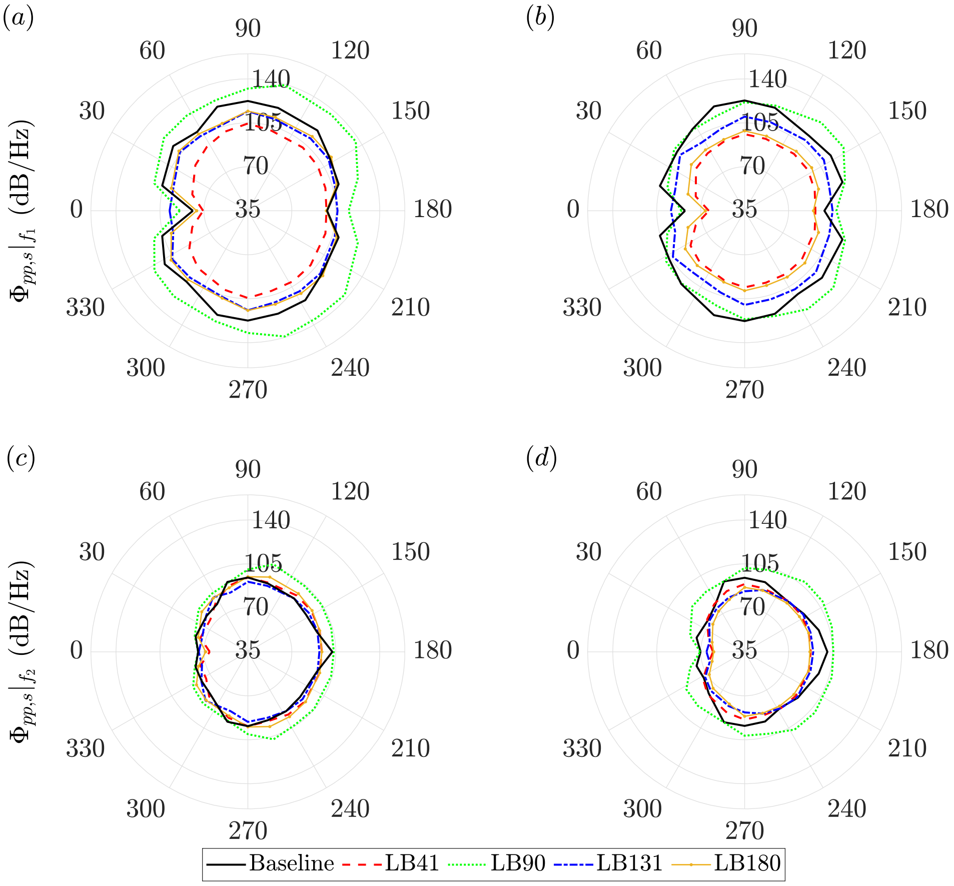

Figure 9: Directivity pattern of the near-field pressure PSD, $\Phi_{pp,s}$ (dB/Hz), at the f_1- and f_2-tone frequencies, i.e., $\Phi_{pp,s}|_{f_1}$, and $\Phi_{pp,s}|_{f_2}$, respectively. (a, c) $C_\mu = 0.003$ ($Re = 1.04 \times 10^5$) and (b, d) $C_\mu = 0.036$ ($Re = 0.7 \times 10^5$). Flow is from left to right.

f_2-tones with respect to the x-axis. In Figs. 9(a) and 9(b), the baseline case exhibits a dipole directivity pattern with an f_1-tone magnitude of approximately 80 dB at $\theta = 0^\circ$ for both $C_\mu = 0.003$ and 0.036. As the peripheral angle increases away from the stagnation point on the top half side of the cylinder, the f_1-tone magnitude reaches a maximum value ($\Phi_{pp,s}|_{f_1} \approx 120$ dB) at $\theta \approx 73^\circ$ and then tends to decrease up to $\theta = 180^\circ$, where $\Phi_{pp,s}|_{f_1}$ becomes entirely broadband in line with the findings of several investigations [2–5, 22, 38, 40]. For all LB cases, the peripheral variation of $\Phi_{pp,s}|_{f_1}$ is similar to that of the baseline, with some noteworthy differences. LB90, for example, displays its maximum $\Phi_{pp,s}|_{f_1}$ at $\theta \approx 106^\circ$ and exhibits a dipole directivity pattern. Additionally, it is observed that increasing C_μ from 0.003 to 0.036 results in a decrease in the f_1-tone magnitude in all LB cases. LB41, in comparison to other LB cases, demonstrates a significant reduction in the f_1-tone magnitude from that of the baseline at $C_\mu = 0.003$, with an average reduction of 23–25 dB, specifically within $\theta \approx 16^\circ$–41°. LB90, on the other hand, exhibits the opposite behaviour, especially on the leeward side of the cylinder. At $C_\mu = 0.036$, both LB41 and LB180 show the same reduction in the f_1-tone magnitude, while LB90 presents an f_1-tone magnitude that is approximately similar to that of the baseline, except within $\theta \approx 106^\circ$–163°.

Upon observing Figs. 9(c) and 9(d), it becomes apparent that each LB case exhibits a uniform

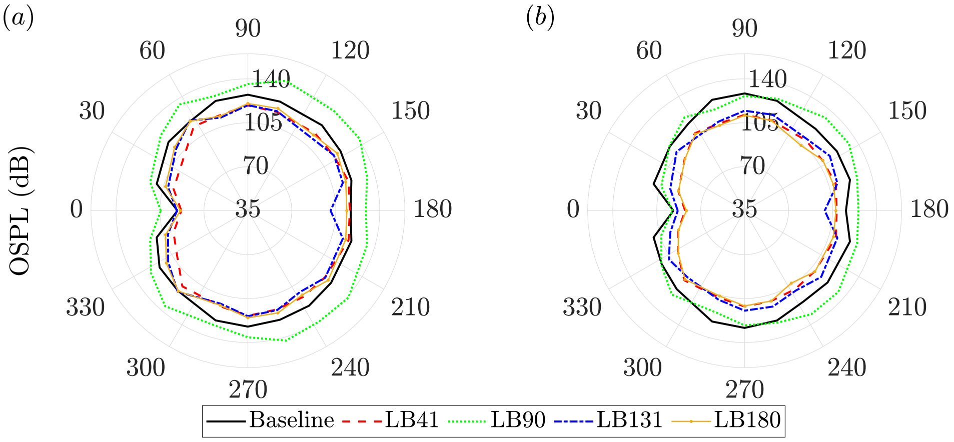

Figure 10: Overall surface pressure level (OSPL) (dB) for (*a*) $C_\mu = 0.003$ and (*b*) 0.036 ($Re = 1.04 \times 10^5$ and 0.7×10^5, respectively). Flow is from left to right.

increase in $\Phi_{pp,s}|_{f_2}$ from $\theta = 0°$ to 180°, following a trend similar to that of the baseline. This observation, in conjunction with the findings in Figs. 9(*a*) and 9(*b*), leads to the following explanations: (*i*) the f_1-tone is maximised around the boundary layer separation point, while the f_2-tone continues to grow into the fully separated flow and peaks at $\theta = 180°$, and (*ii*) the f_2-tone is generated by a different mechanism than the f_1-tone, a consistent observation with other studies [2, 4, 5, 40], and will be further discussed in Sec. 3.3. Based on these directivity results, it can be explained that the near-field pressure radiates sound waves into the far field at the f_2-tone frequency along the flow, whereas it occurs perpendicular to the flow at the f_1-tone frequency. Previous studies [51, 53] have demonstrated that the sound in the far field exhibits a dipole nature, characterised by a predominant fundamental frequency accompanied by several harmonics. In addition, it has been observed that the fundamental tone radiates most strongly in the direction perpendicular to the free stream, while the second harmonic radiates most strongly in the free stream direction. Upon closer examination of Fig. 9(*c*), it is evident that all LB cases, except LB90, do not alter the f_2-tone magnitude compared to the baseline. The LB90 case, on the other hand, shows an increase of up to 14 dB over the baseline, solely on the leeward side of the cylinder. Nevertheless, at the base of the cylinder, LB90 exhibits the f_2-tone with an amplitude closely resembling that of the baseline. In contrast, other LB cases exhibit a comparable trend by diminishing this amplitude by approximately 11.5 dB. At $C_\mu = 0.036$, the f_2-tone magnitude for all cases is slightly smaller than that at $C_\mu = 0.003$. Furthermore, each LB case decreases the f_2-tone magnitude in certain regions around the stagnation ($\theta = 0°$ and 180°) and separation ($\theta \approx 73°$) points. LB90 displays similar behaviour concerning the f_2-tone magnitude around the circumference of the cylinder as it does at $C_\mu = 0.003$, except for some regions around $\theta = 41°$.

To provide a quantitative assessment of the near-field pressure distribution around the cylinder, the Overall Surface Pressure Level (OSPL) (dB) is presented in Fig. 10. The OSPL is obtained by integrating the surface pressure PSD over the frequency range of interest, corresponding to $St \approx 0.13$–13. For the baseline case, the OSPL exhibits a directivity pattern similar to that observed for $\Phi_{pp,s}|_{f_1}$ in Figs. 9(*a*) and 9(*b*), indicating that the overall energy content of the surface pressure fluctuations is primarily contributed by the flow structures generated at the f_1-tone frequency. The directivity pattern of the OSPL is dipole in nature, without any indentation at $\theta = 180°$, where

$\Phi_{pp,s}|_{f_2}$ reaches its maximum magnitude, as shown in Figs. 9(c) and 9(d). Hence, the directivity pattern of the OSPL appears to be a combination or superposition of the directivity patterns observed for $\Phi_{pp,s}|_{f_1}$ and $\Phi_{pp,s}|_{f_2}$ in Fig. 9.

Each LB case exhibits a similar directivity pattern in the OSPL, with the exception of LB131, which consistently displays a dipole pattern at all C_μ values considered, with an indentation at $\theta = 0°$ and $180°$. This observation is in line with the fact that the boundary layer is compressed onto the cylinder surface by the upstream flow [26]. Additionally, the presence of a long distance between the vortex formation region and $\theta = 0°$ can contribute to the lowest OSPL being achieved at this point. By observation in Fig. 10(a), it is evident that each LB case, except LB90, leads to a reduction in the OSPL at $C_\mu = 0.003$. Specifically, LB131 exhibits a greater reduction in comparison to LB41 and LB180, but only at $\theta = 180°$. At $C_\mu = 0.036$, all LB cases show a similar reduction in the OSPL, and this reduction is more pronounced than what was observed at $C_\mu = 0.003$. Meanwhile, LB90 increases the OSPL on the leeward side of the cylinder.

3.3. *Lift and drag spectra*

The PSD of the unsteady lift and drag coefficients, denoted as $\phi_{C_L C_L}$ and $\phi_{C_D C_D}$ (Hz^{-1}), respectively, is presented in Fig. 11 to gain insights into how the LB technique suppresses unsteady forces. The unsteady lift and drag were obtained by integrating the time-dependent surface pressures, which have been measured simultaneously at multiple positions around the circumference of the cylinder, following the established approach used by other researchers [37, 55]. In the subcritical Reynolds-number range, which is the primary focus of the present study, the contribution of friction drag (skin friction) is entirely negligible, representing less than 2% of the total drag, as reported by Achenbach [54] and Fage et al. [56]. Neglecting wall friction, the instantaneous lift, F_L (N), and drag, F_D (N), were calculated as introduce by Maryami and Ali [40] using the following expressions:

$$F_L(t) = \frac{D}{2}\int_0^{2\pi} p(t,\theta)\,\sin\theta\,\mathrm{d}\theta, \tag{6}$$

$$F_D(t) = \frac{D}{2}\int_0^{2\pi} |p(t,\theta)\,\cos\theta|\,\mathrm{d}\theta \tag{7}$$

Using the same method as discussed in detail in Sec. 2.3 for the near-field pressure and far-field noise spectra, the PSD of lift and drag was calculated, and the relevant coefficients were derived as follows:

$$\phi_{C_L C_L} = \frac{\phi_{LL}}{(0.5\rho U_\infty^2)^2}, \tag{8}$$

$$\phi_{C_D C_D} = \frac{\phi_{DD}}{(0.5\rho U_\infty^2)^2} \tag{9}$$

The results depicted in Fig. 11 reveal the prominent tonal peaks at the f_1- and f_2-tone frequencies in the spectra of $\phi_{C_L C_L}$ and $\phi_{C_D C_D}$, respectively, for the baseline case, which is consistent with findings from other studies [2, 4, 5, 22, 38, 40, 51, 52]. The dominant tonal frequency of $\phi_{C_D C_D}$ is twice that of $\phi_{C_L C_L}$ because vortices shed from both sides of the cylinder

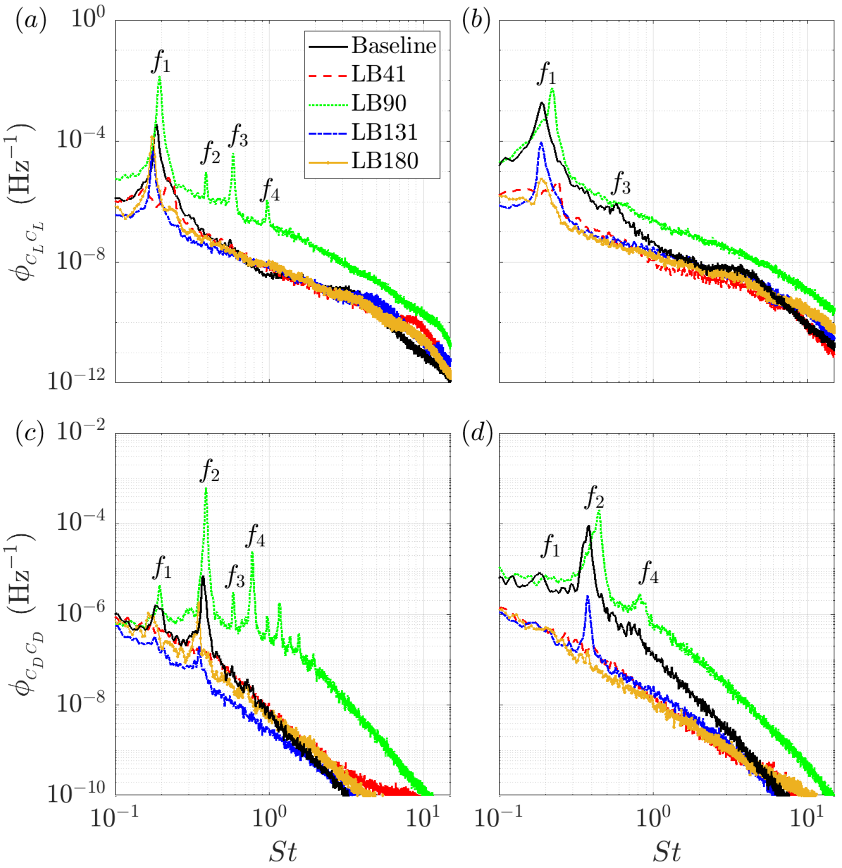

Figure 11: Lift and drag coefficient PSDs, $\phi_{C_L C_L}$ and $\phi_{C_D C_D}$ (Hz^{-1}), respectively, as a function of St. (a, c) $C_\mu = 0.003$ ($Re = 1.04 \times 10^5$) and (b, d) $C_\mu = 0.036$ ($Re = 0.7 \times 10^5$).

contribute equally to drag but have opposite contributions to lift [2]. Furthermore, the spectra of $\phi_{C_L C_L}$ and $\phi_{C_D C_D}$ exhibit tonal behaviour similar to the near-field pressure spectra at $\theta = 90°$ and 180°, respectively (see Figs. 8(a_3) and 8(a_5)). These observations align with previous findings [2, 4, 5, 22, 38, 40], indicating that fluctuating pressures acting on the surface of the cylinder, except for the rearmost part, contribute significantly to lift fluctuations, with energy concentrated in a band around the f_1-tone frequency [1]. On the other hand, surface pressure fluctuations at the base of the cylinder ($\theta = 180°$) contribute to drag fluctuations at the f_2-tone frequency. Notably, the magnitude of the main tone in the $\phi_{C_L C_L}$ spectrum exceeds that of the $\phi_{C_D C_D}$ spectrum, indicating the dominance of lift fluctuations due to the periodic vortex shedding, which constitutes the primary source of cross-stream flow-induced vibration and acoustic emissions [37].

At $C_\mu = 0.003$, as shown in Figs. 11(a) and 11(c), only LB90 demonstrates an increase in the magnitude of the main tones compared to the baseline, consistent with the observations in Figs. 8(a_1)–8(a_5). As demonstrated by Maryami et al. [22], LB90 induces a strong counter flow, primarily attributed to the increased uplift momentum on the top and bottom sides of the cylinder. This effect brings the tails of the separated shear layers closer together, facilitating their interaction in proximity to the cylinder. Consequently, vortex shedding in LB90 occurs nearer to the cylinder compared to the baseline. This closer shedding induces stronger near-field pressure fluctuations and, as a result, more energetic unsteady lift and drag. Conversely, LB41 exhibits a substantial reduction in these tone magnitudes, attributed to the suppression of vortex shedding. Specifically, its f_1-tone in the $\phi_{C_L C_L}$ spectrum is reduced by at least two orders of magnitude relative to the baseline, and its f_2-tone disappears completely in the $\phi_{C_D C_D}$ spectrum. In terms of broadband spectral content, LB90 still tends to exhibit a significant high-frequency contribution compared to the baseline, while other LB cases show a content level similar to the baseline at $C_\mu = 0.003$.

By increasing C_μ to 0.036, the effectiveness of each LB, except LB131, in suppressing lift and drag fluctuations at the dominant tonal frequencies improves, as shown in Figs. 11(b) and 11(d). While LB131 reduces the magnitude of these tones compared to the baseline, they are still larger in magnitude than those at $C_\mu = 0.003$. LB90 exhibits an opposite behavior; the tonal peaks remain larger in magnitude than those of the baseline, but this difference is not as significant as observed at $C_\mu = 0.003$. As the best cases, LB41 and LB180 reveal similar reductions in the tonal peaks of the $\phi_{C_L C_L}$ and $\phi_{C_D C_D}$ spectra at $C_\mu = 0.036$. Interestingly, the $\phi_{C_D C_D}$ spectra for LB41 and LB180 become broadband over the Strouhal number range, indicating that the minimum pressure imposed in the depression area behind the cylinder is transferred downstream by these LB cases to create a smaller pressure difference between the front and rear sides of the cylinder. Greco et al. [57] demonstrated that the depression region reaches its lowest value in the zones where the time-averaged footprints of the von Kármán vortices are located.

3.4. Auto-correlation analysis

This study employs auto-correlation analysis, represented as R_{p_i,p_i}, in conjunction with PSD analysis to examine the primary time scales within the flow. PSD analysis identifies dominant frequencies of surface pressure fluctuations, especially those linked to vortex shedding from a circular cylinder. On the other hand, auto-correlation uncovers the temporal behaviour and periodic patterns of pressure fluctuations, offering valuable insights into the flow dynamics and its time-dependent characteristics [3, 22, 38, 58]. Auto-correlation is calculated as follows:

$$R_{p_i,p_i}(\tau) = \frac{\overline{p_i^{'}(t+\tau)p_i^{'}(t)}}{p_{i_{\rm rms}}^2} \tag{10}$$

where $p_i^{'}$ is fluctuating surface pressure, τ is the time delay, the time average is represented by the overbar, and rms denotes root-mean-square. In the current study, raw data was specifically chosen for auto-correlation calculations, given its nature of investigating the relationship between a signal and itself. Unlike analyses aiming to reveal the magnitude of the signal in the time domain, auto-correlation's focus on this relationship made calibration unnecessary for the calculations.

In Figure 12, the auto-correlation of surface pressure fluctuations is presented in terms of normalised time delay ($\tau^* = \tau U_\infty/D$). At $C_\mu = 0.003$, illustrated in Figs. 12(a_1)–12(a_5), both LB41 and LB180 at $\theta = 0°$ exhibit no discernible periodic behaviour within $-10 < \tau^* < 10$, mirroring the baseline. However, the other LB cases, particularly LB90, manifest strong oscillations with a slow decay rate, showcasing a slight reduction in peak and trough amplitudes of R_{p_i,p_i} concerning τ^*. Note that a slow decay rate implies that surface pressure fluctuations lose their energy content at a slower rate over time [3, 22, 38, 58], allowing them to efficiently scatter acoustic waves to the far field [22, 38], as demonstrated in Fig. 13. Conversely, a fast decay rate implies the opposite behaviour. Notably, LB90 exhibits distinctive oscillations with a time period of $\tau_2^* \approx 2.6$, aligning

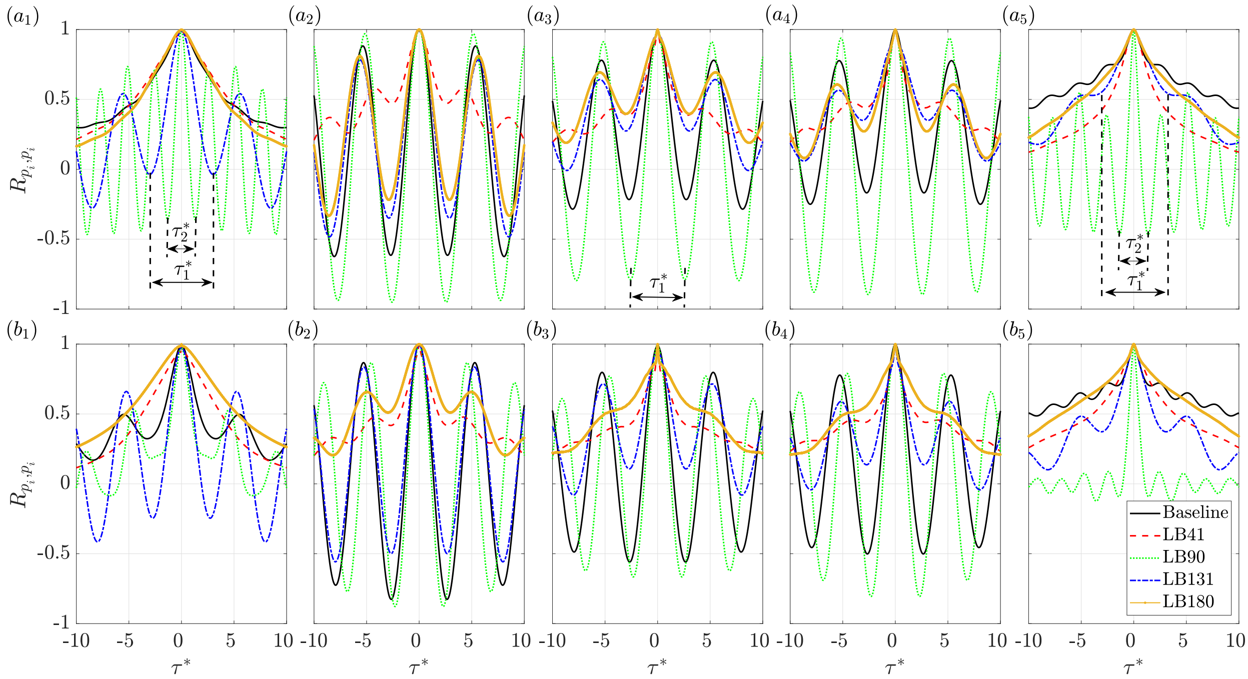

Figure 12: Auto-correlation of the surface pressure fluctuations, R_{p_i,p_i}, measured at (a_1, b_1) $\theta = 0°$, (a_2, b_2) 41°, (a_3, b_3) 90°, (a_4, b_4) 131°, and (a_5, b_5) 180°. (a_1–a_5) $C_\mu = 0.003$ ($Re = 1.04 \times 10^5$) and (b_1–b_5) $C_\mu = 0.036$ ($Re = 0.7 \times 10^5$).

with the f_2-tone frequency, as illustrated in Fig. 12(a_1). Meanwhile, LB131 displays oscillations with a periodicity of $\tau_1^* \approx 5.6$, corresponding to the f_1-tone frequency.

At $\theta = 41°$, 90°, and 131°, as shown in Figs. 12(a_2)–12(a_3), each LB case exhibits periodic behaviour with a time period of τ_1^* similar to the baseline. This suggests that surface pressure fluctuations in the pre-and post-separation region, particularly close to the cylinder's shoulders, are primarily imposed by vortex shedding at the f_1-tone frequency, consistent with the observations in Figs. 8(a_2)–8(a_4). The periodicity corresponding to τ_1^* for LB cases is observed to exhibit slight variations from that of the baseline ($\tau_1^* \approx 5.3$), which aligns with the Strouhal number shift as shown in Fig. 6(b). At $\theta = 41°$ as depicted in Fig. 12(a_2), LB41 demonstrates a weak periodic behaviour with a notably faster decay rate compared to the baseline. Contrarily, other LB cases display robust oscillations in periodic behaviour, with LB90 being the only exception, revealing a slower decay rate compared to the baseline. This implies that LB41 effectively suppresses vortex shedding more than other LB cases, while LB90 does not. Therefore, in the case of LB41, pressure fluctuations imposed by vortex shedding on the cylinder surface quickly lose their energy content over time. Circumferentially moving around the cylinder, the decay rate of each LB slightly increases at $\theta = 90°$ and 131° (see Figs. 12(a_3) and 12(a_4), respectively) and then undergoes rapid decay at $\theta = 180°$ as shown in Fig. 12(a_5). At $\theta = 180°$, each case exhibits oscillation behaviour akin to that observed at $\theta = 0°$ but with an increased decay rate relative to the baseline. Additionally, there is an exception in the case of the baseline, where a faint oscillation with a periodicity corresponding to τ_2^* is noted. At this angle, while LB41 lacks an oscillation similar to LB180, its R_{p_i,p_i} tends to reach zero faster than that of LB180.

As C_μ increases, the decay rate and periodic shape of each LB scheme vary, as depicted in Figs. 12(b_1)–12(b_5). For some LB cases, especially LB90, the decay rate increases, and a weak periodic behaviour with a periodicity corresponding to τ_1^* appears. However, for LB131, a strong periodic shape with a slow decay rate is still observed, specifically at $\theta = 0°$. At $C_\mu = 0.036$, neither LB41 nor LB180 displays periodic behaviour at $\theta = 0°$ and 180°. However, the R_{p_i,p_i} of the LB41 case tends to approach zero more rapidly than that of LB180 and the baseline. At $\theta = 41°$, 90°, and 131°, each LB case exhibits a decaying periodic behaviour, yet LB41 and LB180 showcase a subtle oscillation with a faster decay rate compared to the other LB configurations.

3.5. Near-to-far-field coherence

To investigate the far-field propagation effects of the identified surface pressure fluctuations, the coherence between the near-field pressure sensors and the far-field microphone was computed as follows:

$$\gamma^2_{p_i,p_j} = \frac{|\phi_{p_ip_j}(f)|^2}{\phi_{p_ip_i}(f)\phi_{p_jp_j}(f)} \tag{11}$$

where $\phi_{p_ip_j}$ denotes the cross-spectrum between the near-field pressure and far-field acoustic signals, i.e., $p_i^{'}$ and $p_j^{'}$, respectively, and $\phi_{p_ip_i}$ is the auto-spectrum of each individual signal.

Figure 13 illustrates the near-to-far-field coherence for selected peripheral angles and C_μ values. As expected, the baseline exhibits a high coherence value at the f_1-tone frequency, which is consistent with the f_1-tones observed in Figs. 5 and 8. This indicates that the sound waves are primarily generated by the pressure fluctuations imposed on the cylinder surface through periodic vortex shedding, and then propagate into the far field. From Fig. 13(a_1), the baseline shows coherence value at the f_1-tone frequency with a magnitude near 0.3 at $\theta = 0°$. The magnitude of this tone increases abruptly to around 0.8 when the peripheral angle reaches $\theta = 41°$ and remains constant beyond $\theta = 41°$ up to $\theta = 131°$ as shown in Figs. 13(a_2)–13(a_4). After which, it decreases to zero at $\theta = 180°$, where at the base of the cylinder (see Fig. 13(a_5)). This trend is consistent with previous studies [22, 38, 50, 59, 60], indicating that surface pressure fluctuations induced by vortex shedding in the pre- and post-separation regions, specifically close to the shoulders of the cylinder, contribute significantly to the tonal noise.

This conclusion is valid for the LB cases; however, LB41 provides a significant reduction in the f_1-tone magnitude relative to the baseline within $\theta = 41°$–131° as shown in Figs. 13(a_2)–13(a_4). This indicates that LB41 is capable of propagating acoustic waves with low energy content to the far field by inducing weak surface pressure fluctuations, consistent with the observations in Figs. 5(d) and 8(a_2)–8(a_4), respectively. On the other hand, LB90 shows the opposite behaviour, indicating that this LB case increases far-field noise at the f_1-tone frequency by generating strong near-field pressure. As for LB131 and LB180, it is observed that the coherence at the f_1-tone frequency is almost at the same level as the baseline.

At $C_\mu = 0.036$ and within $\theta = 41°$–131°, the coherence value at the f_1-tone frequency decreases for each LB case (see Figs. 13(b_2)–13(b_4)). However, for LB131, the f_1-tone does not show significant variation with respect to C_μ. It is evident that LB90 and, specifically, LB131 exhibit the f_1-tone with a magnitude larger than that of the baseline. Previous experiments [14, 22, 61, 62] have observed the concept of feedback signals in the context of vortex shedding from a circular cylinder. The exact mechanism remains uncertain, with ongoing discussions regarding whether induced velocity fields of vortices or upstream-traveling vorticity waves are responsible [14]. In

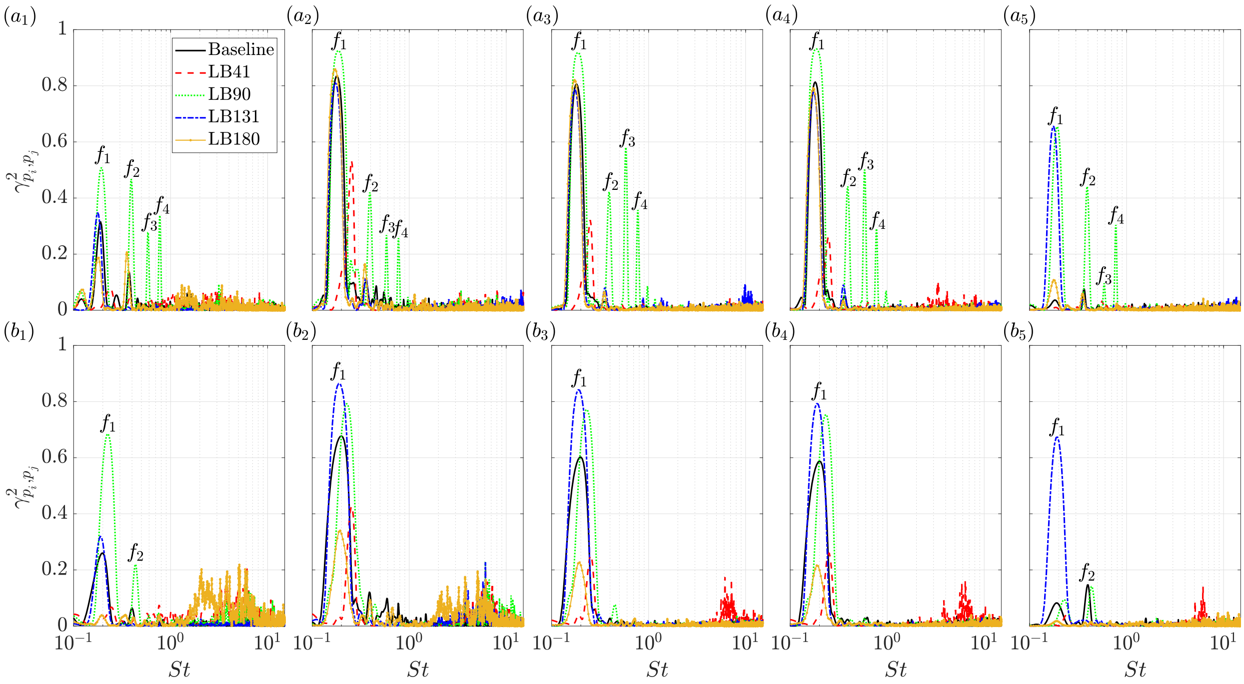

Figure 13: Near- to far-field coherence, $\gamma^2_{p_i,p_j}$, in terms of St for the pressure taps at (a_1, b_1) $\theta = 0°$, (a_2, b_2) 41°, (a_3, b_3) 90°, (a_4, b_4) 131°, and (a_5, b_5) 180°. (a_1–a_5) $C_\mu = 0.003$ ($Re = 1.04 \times 10^5$) and (b_1–b_5) $C_\mu = 0.036$ ($Re = 0.7 \times 10^5$).

any case, Maryami et al. [22] have highlighted that vorticity dynamics within the wake initially perturb the cylinder's shear layers, leading to further intensification within separated shear layers and the generation of vortices in the wake. These vortices create a feedback signal that influences the cylinder, initiating a cycle that impacts the boundary layer. Given this comprehension, the introduction of additional disturbances by LB131 might potentially modify the observed feedback signals and coherence characteristics in the current experimental scenario. On the other hand, for LB41 and LB180, it is observed that the f_1-tone is nearly eliminated at most peripheral angles, with $\gamma^2_{p_i,p_j} < 0.1$. This can be attributed to a larger vortex formation region, where the hydrodynamic energy field appears further downstream and cannot significantly affect pressure fluctuations on the cylinder surface or in the far field. It is important to note that the energy content of the hydrodynamic field dissipates significantly with distance [22, 63], and the application of some LB cases, especially in the boundary layer (LB41), is more pronounced in this behaviour.

3.6. Wavelet transform analysis

In this study, the wavelet transform was employed to analyse the temporal characteristics of surface pressure fluctuations, along with their associated frequencies, which is not possible to achieve using an FFT alone. The wavelet transform provides valuable insights into the amplitude modulation mechanism associated with tonal peaks generated by vortex shedding. Additionally, it allows for the classification of turbulence characteristics in the flow field that induce surface pressure fluctuations, as demonstrated by Farge [64]. For this purpose, we used the continuous wavelet transform, denoted as $W(a,\tau)$ [5, 22, 38, 40, 64–67], which is defined as follows:

$$W(a,\tau) = \frac{1}{\sqrt{C_\psi}} \int_{-\infty}^{+\infty} p^{'}(t)\psi_{a,\tau}^{*}\left(\frac{t-\tau}{a}\right)\mathrm{d}t \tag{12}$$

where a is the scale dilation parameter corresponding to the wavelet width, $\psi(t)$ is the mother wavelet, $\psi^*((t-\tau)/a)$ is the complex conjugate of the dilated and translated $\psi(t)$, and $C_\psi^{-0.5}$ is a constant that takes the mean value of $\psi(t)$. Based on previous studies [5, 22, 38, 40, 64, 67], Morlet was chosen as the mother wavelet in this study.

Figure 14 presents contour plots of the wavelet coefficient modulus, $|W|$, for all LB cases at the selected angles, specifically for $C_\mu = 0.003$. In the baseline case, as shown in Figs. 14(a_2)–14(a_4), at $\theta = 41°$, $90°$, and $131°$, the temporal characteristics of surface pressure fluctuations exhibit amplitude modulation around the f_1-tone frequency, where the highest energy level in surface pressure fluctuations dominates due to vortex shedding. However, within time intervals approximately $t \approx 0.2$–0.25, 0.4–0.5, and 0.85–0.9 s, the $|W|$ level is low, indicating weak vortex shedding during these periods. At $\theta = 0°$ and $180°$, the baseline shows no peaks or amplitude modulation in the time-frequency domain in Figs. 14(a_1)–14(a_5), respectively, suggesting that the alternating shedding of vortices predominantly influences surface pressure fluctuations on the shoulders of the cylinder rather than its front and rear sides.

From Figs. 14(b_1)–14(b_5), it is evident that LB41 suppresses fluctuations at the f_1-tone frequency at all angles, indicating its prominent role in mitigating vortex shedding. In contrast, LB90 exhibits strong amplitude modulation with a high energy level at the f_1-tone frequency over the range of time at $\theta = 41°$, $90°$, and $131°$ (see Figs. 14(c_2)–14(c_4)). Additionally, at the front and rear stagnation points, LB90 shows a strong amplitude modulation at the f_2-tone frequency, with greater fluctuations observed at $\theta = 180°$, consistent with the increased drag fluctuations in Fig. 11(c). For the other two LB cases, the dominant mode at the f_1-tone frequency modulates over time but with a very low energy content. Among all LB cases, only LB131 shows the footprint of weak amplitude modulation at the f_1-tone frequency and $\theta = 0°$ over the time ranges of $t \approx 0$–0.15, 0.2–0.5, and 0.6–0.9 s, indicating the effects of vortex shedding as a hydrodynamic field at the stagnation point.

To analyse the characteristics of the turbulent field responsible for imposing surface pressure fluctuations, the real part of the wavelet coefficients, $\mathbb{R}(W)$, at $C_\mu = 0.003$ is presented in Fig. 15. The results are shown over a short time range of 0.4 seconds to better visualise the turbulent field patterns. At first glance, the patterns of all tested cases can be predominantly categorised into two characteristic classes: repetitive and cone-like patterns. As demonstrated by Farge [64], the turbulent field can be regarded as a superposition of eddies and localised coherent flow structures when the corresponding classes are repetitive and cone-like patterns, respectively. Specifically, Figs. 15(a_1)–15(a_5) reveal that the vortex shedding at the f_1-tone frequency appears as multiple repetitive patches at $\theta = 41°$, $90°$, and $131°$. On the other hand, at $\theta = 0°$ and especially $180°$, only cone-like patterns with different sizes emerge. These observations, in conjunction with the findings in Figs. 14(a_1)–14(a_5), suggest that the repetitive patches in the pre- and post-separation regions represent the effects of large coherent flow structures with high energy content, specifically von Kármán vortices.

As expected for LB41, repetitive patches are not observed at all peripheral angles. This suggests that coherent structures are pushed further downstream by LB41, and their energy content is rapidly dissipated, preventing them from imposing strong surface pressure fluctuations. The

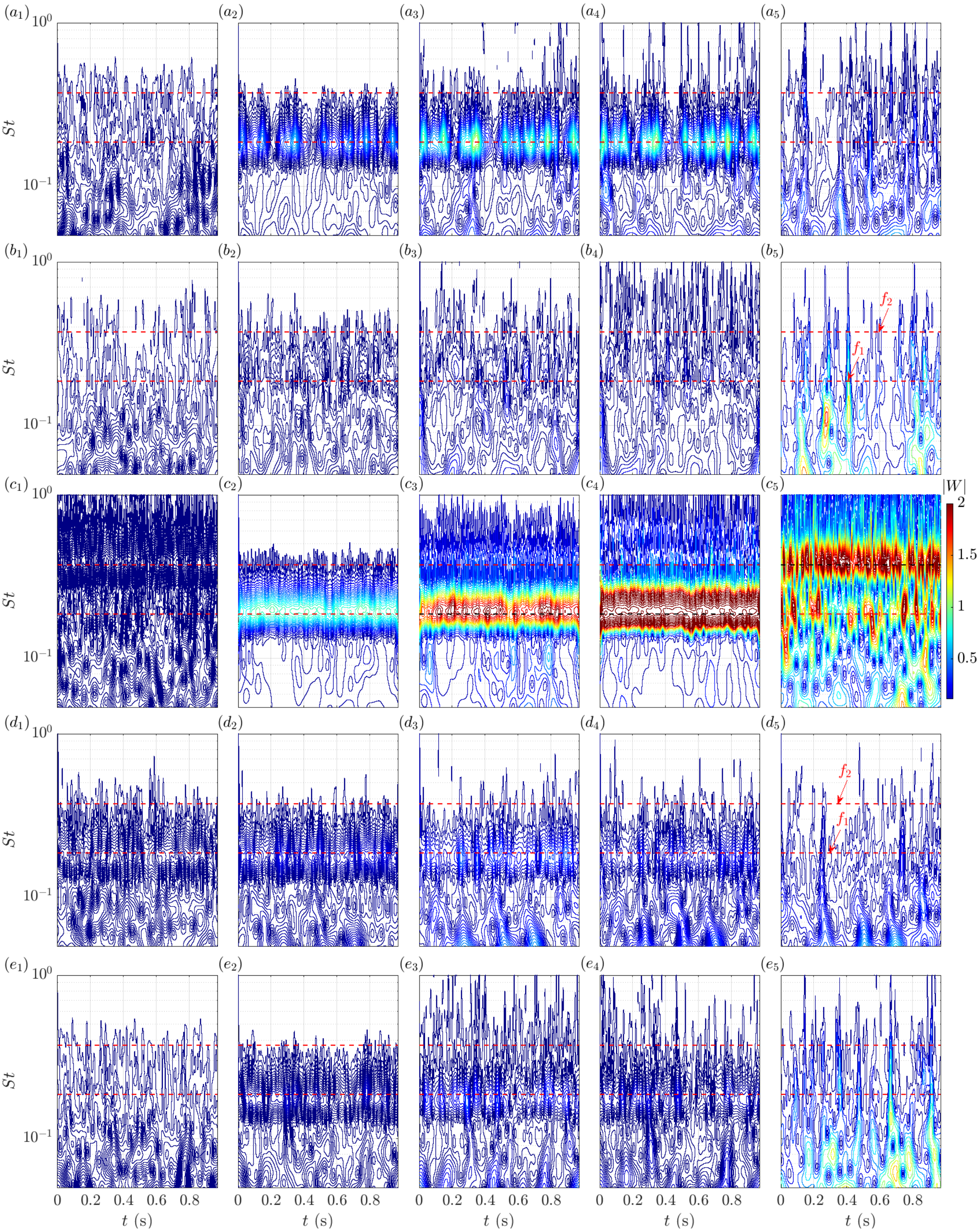

Figure 14: Wavelet scalogram, $|W|$, at (a_1, ..., e_1) $\theta = 0°$, (a_2, ..., e_2) 41°, (a_3, ..., e_3) 90°, (a_4, ..., e_4) 131°, and (a_5, ..., e_5) 180°. (a_1–a_5) Baseline, (b_1–b_5) LB41, (c_1–c_5) LB90, (d_1–d_5) LB131, and (e_1–e_5) LB180. Here, $C_\mu = 0.003$ and $Re = 1.04 \times 10^5$.

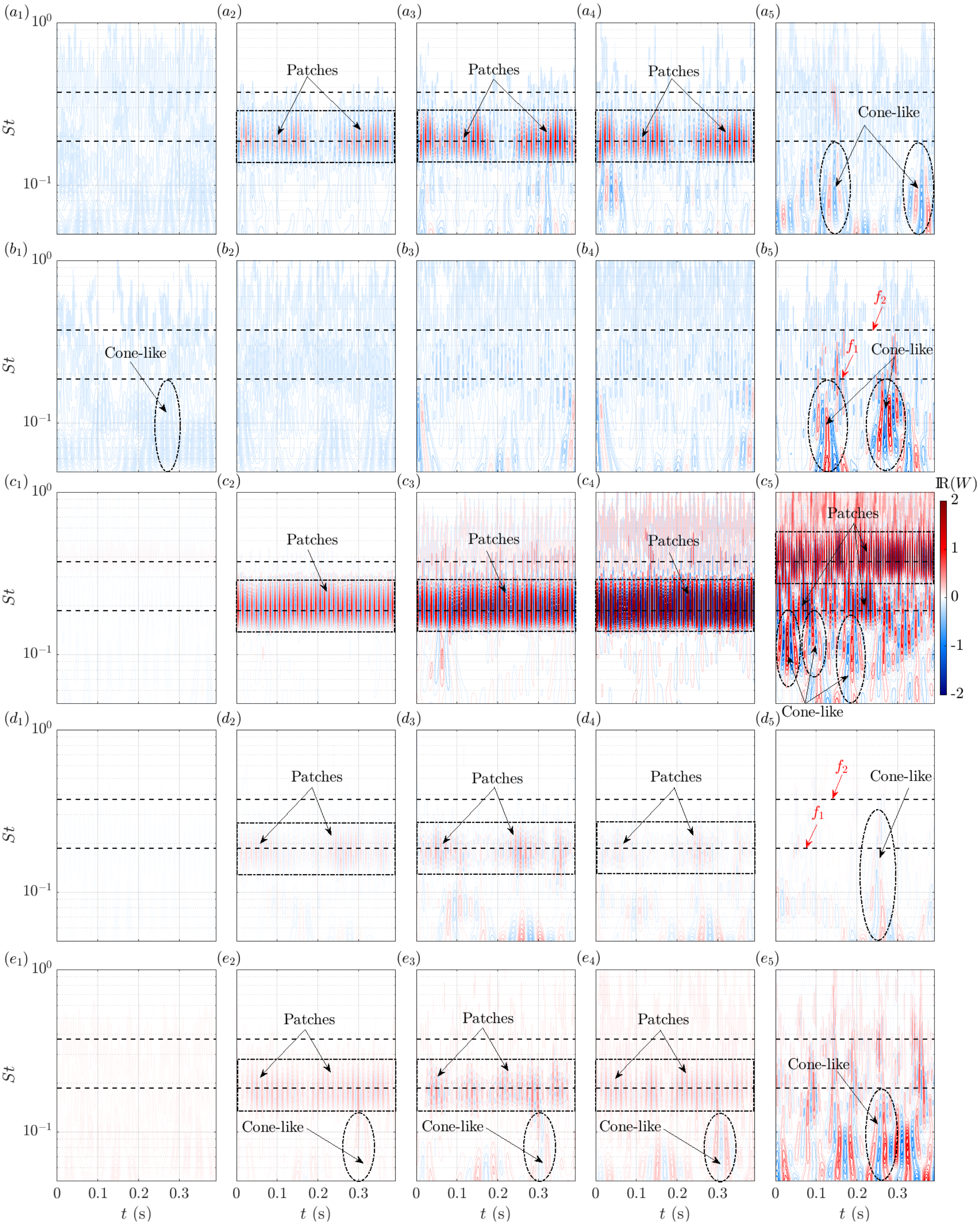

Figure 15: The real part of the wavelet coefficient, $\mathbb{R}(W)$, at (a_1, ..., e_1) $\theta = 0°$, (a_2, ..., e_2) 41°, (a_3, ..., e_3) 90°, (a_4, ..., e_4) 131°, and (a_5, ..., e_5) 180°. (a_1–a_5) Baseline, (b_1–b_5) LB41, (c_1–c_5) LB90, (d_1–d_5) LB131, and (e_1–e_5) LB180. Here, $C_\mu = 0.003$ and $Re = 1.04 \times 10^5$.

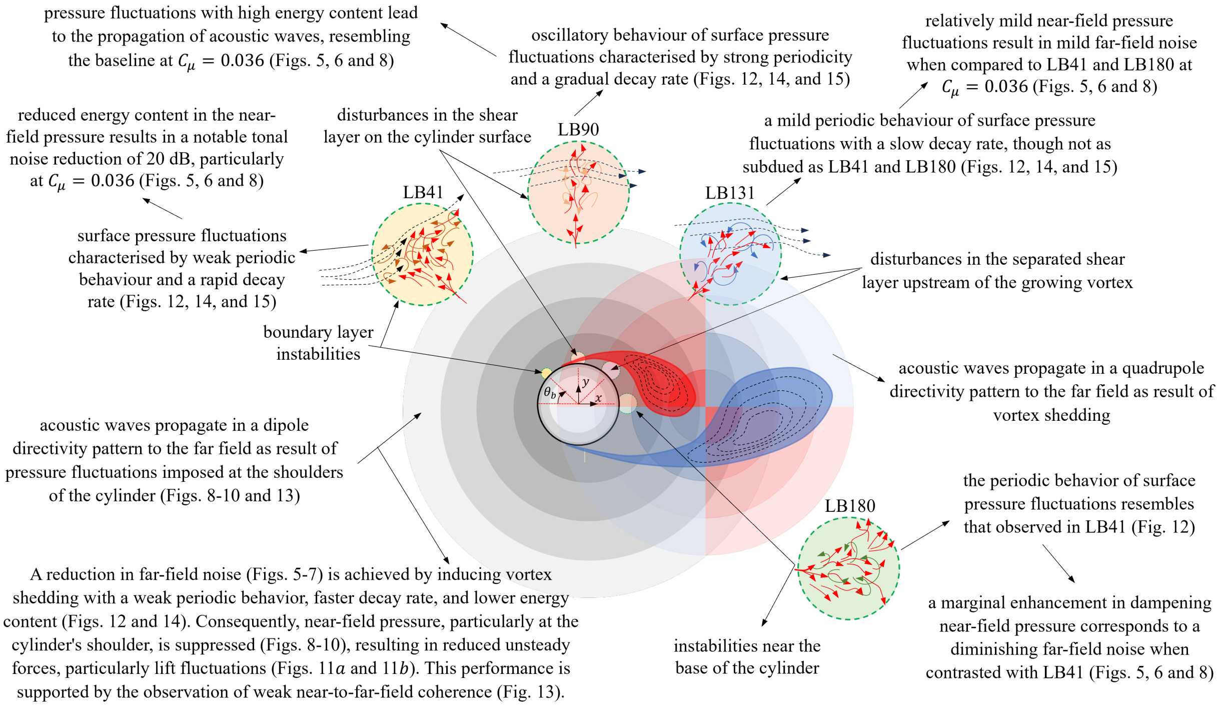

Figure 16: The conceptual flow pattern elucidating the influence of varying LB configurations on surface pressure, and noise generation.

turbulent field classes for LB90, however, are similar to those of the baseline with some notable exceptions. The amplitude of $\mathbb{R}(W)$ shows that the coherent structures possess higher energy content in the case of LB90 compared to the baseline. Additionally, at $\theta = 0°$ and $180°$, LB90 presents strong repetitive patches at the f_2-tone frequency, which is evidence of increased drag (see Fig. 11(b)). For LB131 and LB180, the distribution of energy density among repetitive patches and cone-like patterns is observed at $\theta = 41°$, $90°$, and $131°$, similar to that observed for the baseline. However, the energy levels for LB131 and LB180 are lower compared to the baseline.

4. Conclusion

This study presents an experimental investigation of local blowing applied to a circular cylinder in uniform flow, aiming to assess the noise reduction capability of LB at various circumferential angles. The LB cases were implemented at four peripheral angles ($\theta_b = \pm 41°$, $\pm 90°$, $\pm 131°$, and $180°$) along the $7D$ span of the cylinder, considering three blowing flow rates, and two Reynolds numbers corresponding to $C_\mu = 0.007$–0.036 ($Re = 0.7 \times 10^5$) and $C_\mu = 0.003$–0.016 ($Re = 1.04 \times 10^5$). Experimental data were collected in an anechoic wind tunnel, simultaneously measuring near- and far-field pressure signals. The near-field pressure was obtained using remote sensing methods and several pressure taps distributed at different peripheral locations around the circumference of the cylinder. A summary of the findings in the present study is presented in the schematic diagram shown in figure 16.

Across the range of $C_\mu = 0.007$–0.036 at $Re = 0.7 \times 10^5$, all LB cases, with the exception of LB90, displayed the ability to mitigate vortex shedding noise at the f_1-tone frequency. Notably, LB41 and LB180 exhibited significant noise reduction, reaching around 19 dB at $C_\mu = 0.007$. This noise reduction trend improved as C_μ increased, particularly for LB180, where the reduction reached 23 dB at $C_\mu = 0.036$. Within this range of C_μ values, the effectiveness of LB180 in reducing OASPL was remarkably pronounced, especially when compared to LB41. The investigation drew attention to the influence of additional noise introduced by LB at higher frequencies, a phenomenon more pronounced in LB41 compared to LB180, thus contributing to the differentiation in OASPL reduction between these two LB cases. Notably, the vortex shedding Strouhal number exceeded that of the baseline for LB41 and LB90, while the converse pattern was evident for the other LB cases. Across the range of C_μ values spanning from 0.003 to 0.016, each LB case, except for LB90, still demonstrates a reduction in the magnitude of the f_1-tone in comparison to the baseline. However, this reduction is not as substantial as that observed within the $C_\mu = 0.007$–0.036 range, with values ranging from 5 to 8 dB depending on the specific LB configuration. In contrast, LB90 experiences an increase in the f_1-tone magnitude of approximately 14 dB at $C_\mu = 0.003$, which subsequently decreases to 9 dB as C_μ is raised to 0.016.

The near-field pressure spectra demonstrated the significant impact of LB41 in suppressing the f_1-tone at $C_\mu = 0.003$, particularly around $\theta = 41^\circ$. Surprisingly, both LB41 and LB180 exhibited the same level of f_1-tone reduction as the best cases at $C_\mu = 0.036$, effectively suppressing unsteady forces acting on the cylinder surface. The analysis of near-to-far-field coherence revealed a strong correlation between near-field pressure and far-field noise at the f_1-tone frequency, indicating that the tonal noise is primarily caused by pressure fluctuations induced by vortex shedding on the cylinder's surface. Moreover, the coherence results indicated that periodic pressure fluctuations at the shoulders of the cylinder significantly contributed to the far-field sound waves. The coherence level was lowest for LB41 at the f_1-tone frequency near the shoulders of the cylinder and completely eliminated at the higher C_μ value, which was attributed to the suppression of vortex shedding. The auto-correlation analysis, which reveals the periodicity of the vortex shedding at the f_1-tone frequency, confirmed that LB41 and to some extent LB180 are capable of suppressing vortex shedding with a weak periodic behaviour and increasing the decay rate. Wavelet transform analysis further highlighted LB41's superior vortex shedding attenuation at the f_1-tone frequency across the entire time domain. Interestingly, no distinct turbulent classes were observed for LB41, while repetitive patches and cone-like patterns were evident for other LB cases, especially LB90.

Acknowledgements

This research was supported by the National Natural Science Foundation of China (Grant Nos. 12111530102 and 12272163), Department of Science and Technology of Guangdong Province (Grant No. 2023B1212060001), and the Natural Science Foundation of Shenzhen Municipality (Stable Support Plan Program, Grant No. 20220814230752003).

References

[1] C. Norberg, Interaction between freestream turbulence and vortex shedding for a single tube in cross-flow, J. Wind. Eng. Ind. 23 (1986) 501–514.

[2] D. Casalino, M. Jacob, Prediction of aerodynamic sound from circular rods via spanwise statistical modelling, J. Sound Vib. 262 (2003) 815–844.

[3] R. Maryami, M. Azarpeyvand, A. Dehghan, A. Afshari, An experimental investigation of the surface pressure fluctuations for round cylinders, J. Fluids Eng. 141 (2019) 061203.

[4] R. Maryami, S. A. Showkat Ali, M. Azarpeyvand, A. Afshari, Turbulent flow interaction with a circular cylinder, Phys. Fluids 32 (2020) 015105.
[5] R. Maryami, S. A. S. Ali, M. Azarpeyvand, A. A. Dehghan, A. Afshari, The influence of cylinders in tandem arrangement on unsteady aerodynamic loads, Exp. Therm. Fluid Sci. (2022) 110709.
[6] M. Zdravkovich, Review and classification of various aerodynamic and hydrodynamic means for suppressing vortex shedding, J. Wind. Eng. Ind. 7 (1981) 145–189.
[7] P. M. Hartwich, E. D. Dickey, A. J. Sclafani, P. Camacho, A. B. Gonzales, E. L. Lawson, R. Y. Mairs, A. Shmilovich, AFC-enabled simplified high-lift system integration study, NASA, 2014.
[8] E. Konstantinidis, S. Balabani, M. Yianneskis, The timing of vortex shedding in a cylinder wake imposed by periodic inflow perturbations, J. Fluid Mech. 543 (2005) 45–55.
[9] G. Artana, R. Sosa, E. Moreau, G. Touchard, Control of the near-wake flow around a circular cylinder with electrohydrodynamic actuators, Exp. Fluids 35 (2003) 580–588.
[10] A. Glezer, M. Amitay, Synthetic jets, Annu. Rev. Fluid Mech. 34 (2002) 503–529.
[11] K. Roussopoulos, Feedback control of vortex shedding at low reynolds numbers, J. Fluid Mech. 248 (1993) 267–296.
[12] H. Wan, S. S. Patnaik, Suppression of vortex-induced vibration of a circular cylinder using thermal effects, Phys. Fluids 28 (2016) 123603.
[13] L. Prandtl, Über flussigkeitsbewegung bei sehr kleiner reibung, Verhandl. III, Internat. Math.-Kong., Heidelberg, Teubner, Leipzig, 1904 (1904) 484–491.
[14] D. R. Williams, H. Mansy, C. Amato, The response and symmetry properties of a cylinder wake subjected to localized surface excitation, J. Fluid Mech. 234 (1992) 71–96.
[15] D. Park, D. Ladd, E. Hendricks, Feedback control of von kármán vortex shedding behind a circular cylinder at low reynolds numbers, Phys. Fluids 6 (1994) 2390–2405.
[16] J. Lin, J. Towfighi, D. Rockwell, Near-wake of a circular cylinder: control, by steady and unsteady surface injection, J. Fluids Struct. 9 (1995) 659–669.
[17] C. Min, H. Choi, Suboptimal feedback control of vortex shedding at low reynolds numbers, J. Fluid Mech. 401 (1999) 123–156.
[18] Y. Delaunay, L. Kaiktsis, Control of circular cylinder wakes using base mass transpiration, Phys. Fluids 13 (2001) 3285–3302.
[19] W.-L. Chen, H. Li, H. Hu, An experimental study on a suction flow control method to reduce the unsteadiness of the wind loads acting on a circular cylinder, Exp. Fluids 55 (2014) 1–20.
[20] Z. Hu, H. Liu, Investigation on vortex shedding and noise control of flow around cylinder by blowing and suction, in: International Conference on Dynamics and Vibroacoustics of Machines (DVM), Samara, Russia, IEEE, 2020, 1–10.
[21] Z. Deng, D. Gao, G. Chen, W.-L. Chen, Active wake control of flow past a circular cylinder with slot jet, J. Aerosp. Eng. 34 (2021) 04021033.
[22] R. Maryami, E. J. Arcondoulis, Y. Liu, Flow and aerodynamic noise control of a circular cylinder by local blowing, J. Fluid Mech. 980 (2024) A56.
[23] R. Maryami, E. Arcondoulis, Y. Liu, Experimental investigation of local blowing for noise and flow control of a circular cylinder, in: AIAA AVIATION 2023 Forum, San Diego, CA, 2023-3742.
[24] R. Maryami, E. Arcondoulis, C. Yang, M. Szoke, Z. Xiang, J. Guo, R. Wei, Y. Liu, Application of local blowing to a structured porous-coated cylinder for flow and noise control, in: 28th AIAA/CEAS Aeroacoustics 2022 Conference, Southampton, UK, 2022-2921.
[25] R. Maryami, E. Arcondoulis, Y. Liu, Aeroacoustic investigation of active base blowing applied to a structured porous cylinder, in: AIAA AVIATION 2023 Forum, San Diego, CA, 2023-3741.
[26] L. Mathelin, F. o. Bataille, A. Lallemand, The effect of uniform blowing on the flow past a circular cylinder, J. Fluids Eng. 124 (2002) 452–464.
[27] J. H. Fransson, P. Konieczny, P. H. Alfredsson, Flow around a porous cylinder subject to continuous suction or blowing, J. Fluids Struct. 19 (2004) 1031–1048.
[28] D. Angland, X. Zhang, M. Goodyer, Use of blowing flow control to reduce bluff body interaction noise, AIAA J. 50 (2012) 1670–1684.
[29] S. Patil, T. T. Ng, Control of separation using spanwise periodic porosity, AIAA J. 48 (2010) 174–187.
[30] H. Yu, Z. Xu, W.-L. Chen, H. Li, D. Gao, Attenuation of vortex street by suction through the structured porous surface, Phys. Fluids 33 (2021) 125101.
[31] M. Guo, Z. Wang, H. Yu, D. Gao, Wake control of a bluff-body via distributed jets over its surface, AIP Adv. 12 (2022) 065025.

[32] S. Dong, G. Triantafyllou, G. Karniadakis, Elimination of vortex streets in bluff-body flows, Phys. Rev. Lett. 100 (2008) 204501.

[33] C. Wang, H. Tang, S. C. Yu, F. Duan, Active control of vortex-induced vibrations of a circular cylinder using windward-suction-leeward-blowing actuation, Phys. Fluids 28 (2016) 053601.

[34] D. Gao, G. Chen, W. Chen, Y. Huang, H. Li, Active control of circular cylinder flow with windward suction and leeward blowing, Exp. Fluids 60 (2019) 26.

[35] J. Kim, H. Choi, Distributed forcing of flow over a circular cylinder, Phys. Fluids 17 (2005) 033103.

[36] Y. Yang, Y. Liu, R. Liu, C. Shen, P. Zhang, R. Wei, X. Liu, P. Xu, Design, validation, and benchmark tests of the aeroacoustic wind tunnel in sustech, Appl. Acoust. 175 (2021) 107847.

[37] C. Norberg, Fluctuating lift on a circular cylinder: review and new measurements, J. Fluids Struct. 17 (2003) 57–96.

[38] R. Maryami, E. J. Arcondoulis, Q. Liu, Y. Liu, Experimental near-field analysis for flow induced noise of a structured porous-coated cylinder, J. Sound Vib. (2023) 117611.

[39] R. Maryami, E. J. Arcondoulis, C. Yang, Y. Liu, Relationship between vortex shedding noise and remotely-sensed surface pressure fluctuations of a structured porous-coated cylinder, in: INTER-NOISE and NOISE-CON Congress and Conference Proceedings, Glasgow UK, 2022, 515–526.

[40] R. Maryami, S. A. S. Ali, Near-field pressure and wake velocity coherence of a circular cylinder, Phys. Fluids 35 (2023).

[41] S. S. Vemuri, X. Liu, B. Zang, M. Azarpeyvand, On the use of leading-edge serrations for noise control in a tandem airfoil configuration, Phys. Fluids 32 (2020) 077102.

[42] R. Maryami, S. A. Showkat Ali, M. Azarpeyvand, Experimental investigation of coherent and turbulent fluid flow interactions with a circular cylinder, in: AIAA AVIATION 2023 Forum, San Diego, CA, 2023, 3743.

[43] M. Gruber, Airfoil noise reduction by edge treatments, Ph.D. thesis, University of Southampton, 2012.

[44] A. Garcia-Sagrado, T. Hynes, Stochastic estimation of flow near the trailing edge of a naca0012 airfoil, Exp. Fluids 51 (2011) 1057–1071.

[45] A. Afshari, M. Azarpeyvand, A. A. Dehghan, M. Szőke, R. Maryami, Trailing-edge flow manipulation using streamwise finlets, J. Fluid Mech. 870 (2019) 617–650.

[46] J. S. Bendat, A. G. Piersol, Random data: analysis and measurement procedures, volume 729, John Wiley & Sons, 2011.

[47] S. A. Showkat Ali, M. Azarpeyvand, C. R. I. Da Silva, Trailing edge bluntness noise reduction using porous treatments, J. Sound Vib. 474 (2020) 115257.

[48] J. Guo, R. Maryami, C. Yang, Y. Yang, X. Wang, Y. Liu, Aerodynamic noise reduction of a blunt flat plate by trailing-edge blowing, Phys. Fluids 35 (2023).

[49] H. E. Bass, L. C. Sutherland, A. J. Zuckerwar, D. T. Blackstock, D. Hester, Atmospheric absorption of sound: Further developments, J. Acoust. Soc. Am. 97 (1995) 680–683.

[50] O. Inoue, N. Hatakeyama, Sound generation by a two-dimensional circular cylinder in a uniform flow, J. Fluid Mech. 471 (2002) 285–314.

[51] B. Etkin, G. Korbacher, R. T. Keefe, Acoustic radiation from a stationary cylinder in a fluid stream (aeolian tones), J. Acoust. Soc. Am. 29 (1957) 30–36.

[52] L. Qin, Development of reduced-order models for lift and drag on oscillating cylinders with higher-order spectral moments, Ph.D. thesis, Virginia Tech, 2004.

[53] J. Gerrard, Measurements of the sound from circular cylinders in an air stream, Proc. Phys. Soc. Section B 68 (1955) 453.

[54] E. Achenbach, Distribution of local pressure and skin friction around a circular cylinder in cross-flow up to $re = 5 \times 10^6$, J. Fluid Mech. 34 (1968) 625–639.

[55] W. Z. Sadeh, D. B. Saharon, Turbulence effect on crossflow around a circular cylinder at subcritical Reynolds numbers, Technical Report, NASA, 1982.

[56] A. Fage, V. Falkner, Further experiments on the flow around a circular cylinder, Technical Report, HM Stationery Office, 1931.

[57] C. S. Greco, G. Paolillo, T. Astarita, G. Cardone, The von kármán street behind a circular cylinder: Flow control through synthetic jet placed at the rear stagnation point, J. Fluid Mech. 901 (2020) A39.

[58] S. A. Showkat Ali, M. Azarpeyvand, C. R. I. Da Silva, Trailing-edge flow and noise control using porous treatments, J. Fluid Mech. 850 (2018) 83–119.

[59] Y. Oguma, T. Yamagata, N. Fujisawa, Measurement of sound source distribution around a circular cylinder in a uniform flow by combined particle image velocimetry and microphone technique, J. Wind Eng. Ind. Aerodyn 118 (2013) 1–11.

[60] S. Li, D. E. Rival, X. Wu, Sound source and pseudo-sound in the near field of a circular cylinder in subsonic conditions, J. Fluid Mech. 919 (2021) A43.

[61] M. Nishioka, H. Sato, Mechanism of determination of the shedding frequency of vortices behind a cylinder at low reynolds numbers, J. Fluid Mech. 89 (1978) 49–60.

[62] M. Unal, D. Rockwell, On vortex formation from a cylinder. part 1. the initial instability, J. Fluid Mech. 190 (1988) 491–512.

[63] T. Suzuki, T. Colonius, Instability waves in a subsonic round jet detected using a near-field phased microphone array, J. Fluid Mech. 565 (2006) 197–226.

[64] M. Farge, Wavelet transforms and their applications to turbulence, Annu. Rev. Fluid Mech. 24 (1992) 395–458.

[65] S. Mallat, A wavelet tour of signal processing, Elsevier, 1999.

[66] H. Li, T. Nozaki, Wavelet analysis for the plane turbulent jet: analysis of large eddy structure, JSME Int. J. Ser. B 38 (1995) 525–531.

[67] D. A. Lysenko, I. S. Ertesvåg, K. E. Rian, Large-eddy simulation of the flow over a circular cylinder at reynolds number 2× 104, Flow Turbul. Combust. 92 (2014) 673–698.